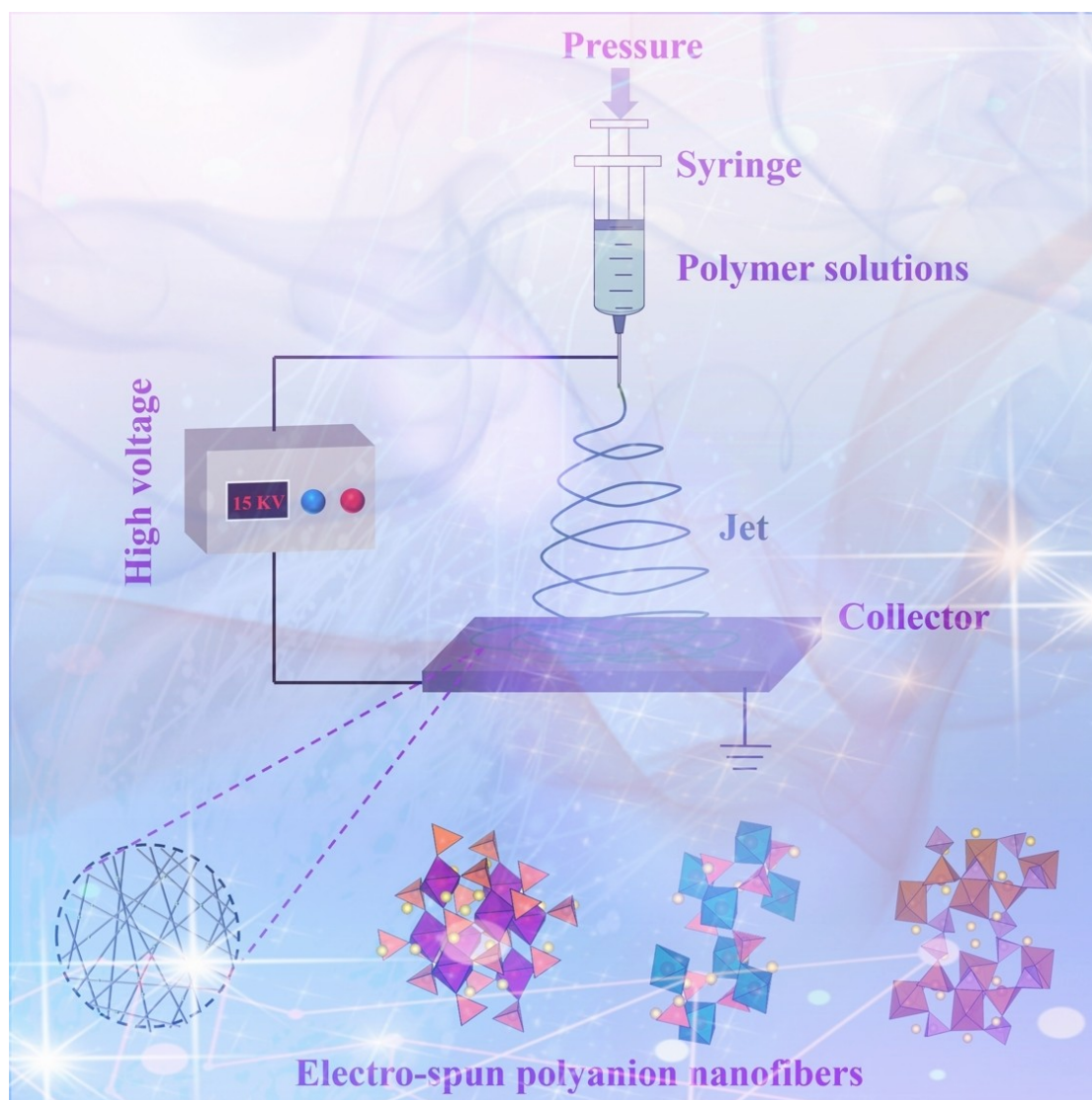# Electrospinning Polyanionic Materials for High-Rate Na Storage

Yi Yang+,[a] Shitan Xu+,[a] Wensun Zhu,[a] Chen Xu,*[b] and Xianhong Rui*[a]

Batteries & Supercaps

Review
doi.org/10.1002/batt.202300271

Chemistry
Europe

European Chemical
Societies Publishing

As emerging energy storage devices, sodium-ion batteries (SIBs) are perceived as promising alternatives to lithium-ion batteries (LIBs) due to their low cost and high safety. The cathodic side plays a crucial role in determining the energy density as well as the service life of SIBs, and the polyanionic cathode materials are featured by excellent cycle stability, flexible operating voltage and suitable overall electrochemical properties. However, the intrinsic inferior electronic conductivity limits their rate performance. Recently, the possibility of employing advanced electrospinning techniques to fabricate polyanionic materials has been explored. The facile electrospinning can greatly facilitate the ionic and electronic conduction of cathodes by constructing three-dimensional (3D) conductive networks with the one-dimensional (1D) nanofibers, and thus improves their electrochemical performance. In this review, we summarize the research progress of the electro-spun polyanionic cathodic materials and their applications in SIBs, and present future prospects as well as challenges of the electro-spun polyanions faced to the ever-increasing demand of advanced energy storage.

1. Introduction

The far-reaching impact of increasingly serious environmental pollution caused by non-renewable fossil fuels make the exploration of energy transformation on the agenda. Recently, energy innovation is responding worldwide and gradually replacing fossil fuels with renewable energy resources like wind power, tidal power, biomass power and photovoltaic power generation. However, the development and utilization of clean energy are greatly limited by complex geography and volatile weather, so the high performance energy storage device support is essential to achieve the efficient use of renewable energy.[1] Having the merit of high energy density and long service life, lithium-ion batteries (LIBs) are now the mainstream energy storage technology, which is widely used in portable electronic devices and electric vehicles.[2] Nevertheless, limited by the scarce reserve of lithium and high development costs, the LIBs are unable to meet the energy storage demands in the future. Therefore, it is crucial to develop the new battery technology to relieve the demand. Both located in the IA family, Na and Li have similar physicochemical properties and ion storage principles. In addition, the standard electrode potential of Na (-2.7 V) is higher than that of Li (-3.04 V), thus SIBs demonstrate more stable electrochemical performance and better safety.[3] In terms of cost, the sodium raw materials are abundantly available in the earth (~1350 times higher than Li) and of lower price;[4] Furthermore, Na does not alloy with Al, thus the inexpensive Al collector can be used as collectors for both cathodes and anodes in SIBs, which further reduce the manufacturing costs.[5] Finally, the assemble of SIBs is similar to the LIBs, which is compatible with existing equipment and has a well-established industrial flow.[6] In brief, SIBs are promising alternatives of LIBs for future applications in large-scale energy storage. However, the Na$^+$ have a larger radius than Li$^+$, resulting in slow diffusion kinetics in electrode materials, which limits the specific capacity and rate performance.[7] Thus, it is of great importance to explore and develop the suitable electrode materials for the SIBs.

At present, transition metal oxides, polyanionic compound, Prussian blue (analogues) and organic compound have been developed as the cathode materials for SIBs.[8] Among them, the layer-structured transition metal oxides have high energy densities and excellent rate performance, while suffer from unstable crystal structure and poor cyclability.[9] The Prussian blue and its analogues have relatively stable structure and good rate performance, but the difficulty in eliminating crystalline water has limited their industrialization.[10] The organic compounds are abundant and of high capacities, but they are easily dissolved in organic electrolytes and suffer from capacity failure.[11] The disadvantages of the cathode materials mentioned above will be exaggerated in large-scale electrochemical energy storage, which is still in its infancy and has high requirements for practicality and economy as well as safety. In contrast, the polyanionic materials with great structural stability and thermal stability are considered to be one of the most promising cathode candidates for practical SIBs. The polyanionic compound consists of an over-metallic octahedron MO_6 (M$=$Fe, Ti, V) and a polyanionic tetrahedron $(XO_4)^{n-}$ (X$=$P, Si, S) with an open 3D framework structure, which is beneficial for the insertion/desertion of the Na$^+$.[12] Furthermore, the strong covalent bonding of X–O ensures the structural stability of polyanionic electrode during cycling. Moreover, the isolated electronic structure of the transition metal ions can generate high operating voltage, but leads to low electronic conductivity of the polyanionic materials, limiting their rate capabilities.[12b] To address this drawback, nanosizing and carbon coating are considered and employed to optimize their ion storage properties. The large specific surface area of nanomaterials offer a large number of active sites for ions and shortens the ion diffusion length, accelerating the insertion/desertion process, and also renders a high tolerance for volume change during cycling.[13] Carbon coating helps enhance the electronic conductivity of the cathode materials and inhibit grain growth.[8b,14]

Nowadays, a wide range of techniques, such as chemical vapor deposition (CVD), sol-gel, spray drying and electrospinning, have been developed for constructing nanostructures.[15] Among them, electrospinning is the primary technique to prepare 1D nanofibers with the superiority of low cost, facile manufacturing equipment, multifidous spinnable option and controllable process.[16] Compared to other methods, electrospinning is facile and versatile. The electro-spun fibers have a variety of morphologies and superior mechanical integrity, and can also be paired with post heat

[a] Y. Yang,[+] S. Xu,[+] W. Zhu, Prof. X. Rui
     School of Materials and Energy
     Guangdong University of Technology
     Guangzhou 510006 (China)
     E-mail: xhrui@gdut.edu.cn

[b] Dr. C. Xu
     Academy for Advanced Interdisciplinary Studies
     Southern University of Science and Technology
     Shenzhen 518055 (China)
     E-mail: xuc3@sustech.edu.cn

[+] These authors contributed equally to this work.

Batteries & Supercaps

Review
doi.org/10.1002/batt.202300271

Chemistry
Europe
European Chemical
Societies Publishing

treatment to achieve carbon encapsulation.[17] In the 1990s, Reneker et al. used electrospinning to prepare polyacrylonitrile (PAN) nanofibers, which were then heat-treated to obtain the carbon nanofibers (CNF). They conducted an in-depth study of the electrospinning process and its applications.[18] It is worth mentioning that carbon nanofibers prepared by electrospinning do not necessarily require the addition of conductive additives and binders, so they are advantageous when being used as electrode materials for SIBs/LIBs. Li et al. presented the structural and compositional evolution of materials fabricated by electrospinning, and discussed in details applications of various electro-spun cathode materials for LIBs and SIBs.[19] Wang et al. discussed the use of electro-spun 1D nanomaterials in advanced Na storage devices, such as SIBs, sodium-sulfur batteries, sodium-selenium batteries, sodium-air batteries and sodium ion capacitor, etc.[20] In 2022, Li et al. described the capability of electrospinning to construct different nanostructures and recent advances in the electro-spun carbon-based hybrids as electrodes for SIBs.[15] About the cathode side, Armer et al. summarized the application of electro-spun vanadium oxides as electrode materials in LIBs, SIBs and AIBs (Al-ion batteries), confirmed the feasibility of using electro-spun vanadium oxides as cathode materials for secondary batteries.[21]

Stemming from the good adaptability of electrospinning technology with the fabrication of polyanionic cathode materials, this review mainly summarizes the research progress of electro-spun polyanionic cathode materials in SIBs, followed by the remaining challenges needed to be overcome for future applications. We hope that this review will contribute to the development of advanced cathode materials for high rate SIBs.

2. Electrospinning

Electrospinning is a fabrication technique in which polymeric solutions or melts are sprayed and stretched under electrostatic force to obtain nanoscale fibers. As early as 1934, Formhals successfully electro-spun the cellulose acetate (CA) solutions under electrostatic force, and filed the first patent of fabricating ultrafine fibers via electrospinning.[20] The development process of electrospinning technology could be divided into four stages: i) investigating the spinnability of different polymers, the influence of process parameters on fiber diameter and properties in the spinning process, and the optimization of process parameters; ii) diversifying electro-spun nanofiber composition and fine regulating its structure; iii) applying the electro-spun fibers in fields such as energy, environment, biomedicine, and optoelectronics; iv) achieving large-scale manufacturing of the electro-spun fibers. As a simple and effective processing technology, electrospinning plays a huge role in catalysis, energy, photoelectric, biomedical, filtration, and other fields.[22] The working principles and devices of electrospinning are uncomplicated. A typical electrospinning machine is generally composed of receiving device, spinneret with metal needle and high-voltage power supply.[23] Among them, the positive and negative electrodes of the high-voltage power supply are connected to the syringe needle and the receiving device, respectively. The receiving device can be a still plane or high-speed rotating roller/disc. During the classical electrospinning procedure, the polymeric solution is loaded into the syringe and enters the spinneret through the pump, where the surface tension of the polymer is in equilibrium with the charged droplets at the end of the spinneret. Afterwards, an increasing pressure is applied between the spinneret and the collection device, and the electrostatic repulsion on the droplet surface causes the droplet to elongate and gradually transform to a conical from spherical. According to Taylor's description, there is a conical half-angle of ~49.3° that puts the liquid cone in mechanical equilibrium, and the cone in this state is called a Taylor cone. As the electric field increases to a critical value, the charge repulsion is greater than the droplet surface tension, and the jet is ejected from the surface of the Taylor cone, undergoing complex bending, elongation and whipping motions while the solvent evaporates. Ultimately, the cured polymer fibers are arranged in a disordered pattern on the receiving device, forming a fiber mat, the diameter of which is generally between tens of nanometers and several micrometers.[24] Different raw materials and electrospinning conditions will result in different morphologies, including core/shell, porous, hierarchical, hollow and fiber-in-tube (Figure 1). In the fabrication process, factors affecting the electrospinning including: 1) Molecular weight and the molecular structure (branching, linearity, etc.) of the polymers; 2) solution properties (concentration, viscosity, conductivity, surface tension, etc.); 3) working voltage magnitude; 4) length between the spinneret and the collection panel; 5) shape of needle at the spinneret; 6) motion mode of the collection component; 7) environmental parameters (e.g., temperature, humidity, air flow, etc.).[16,18,25]

Chen Xu obtained her Bachelor's degree (2010) and PhD degree (2015) in Material Science and Engineering from Nanyang Technological University (NTU), Singapore. From 2015 to 2017, she worked as a research fellow in School of Electrical and Electronic Engineering in NTU. At present, she is a Research Assistant Professor of Academy for Advanced Interdisciplinary Studies, Southern University of Science and Technology. Her current research focuses on the development of advanced energy materials by high-throughput synthesis and characterization.

Xianhong Rui is a professor at Guangdong University of Technology. He received B.S. degree from the University of Jinan in 2007 and M.S. degree from the University of Science and Technology in 2010. He obtained Ph.D. degree from the School of Materials Science and Engineering at Nanyang Technological University in 2014. His research interests mainly focus on the design and fabrication of advanced electrode materials for energy conversion and storage.
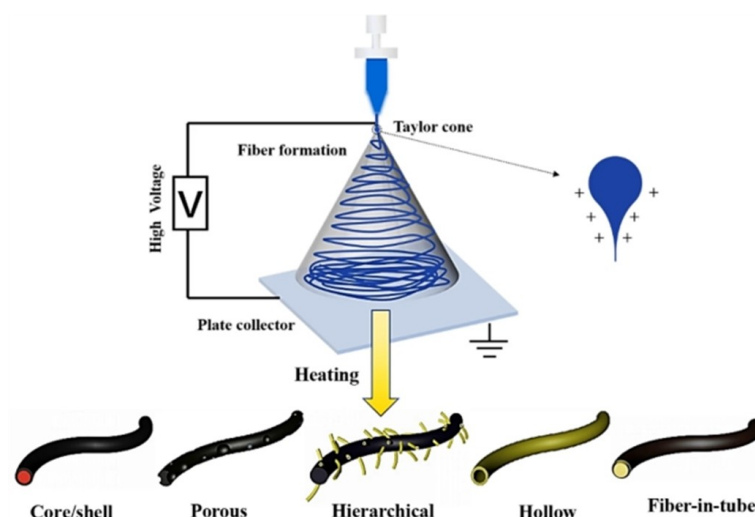
Figure 1. Schematic illustration of the working principle of electrospinning. Reproduced with permission from Ref. [15]. Copyright (2022) Spring Nature.

According to the varying forms of spinning solution, the electrospinning can be divided to the solution electrospinning and the molten electrospinning. The fibers fabricated from solution electrospinning usually have diameters of nanometers with satisfactory stretchability and mechanical properties. However, there are also some shortcomings associated with the solution electrospinning: i) The proportion of polymer in the electrospinning system is only ~10 wt%, resulting in low fabrication efficiency; ii) Some electrospinning systems need to be carried out in highly corrosive or highly toxic solvents; iii) The employed organic solvents are costly, hard to recycle, and not environmentally unfriendly. Melt electrospinning is developed to resolve the above mentioned shortcomings by directly using the raw material melt as the precursors, which offers advantages over solution electrospinning: 1) low cost and high production efficiency without the utilization of organic solvents; 2) suitable for polymers that do not have suitable solvents to dissolve at room temperatures, such as PP, PE;[26] 3) Modeling melt electrospinning is helpful for a deeper understanding of electrospinning mechanisms; 4) It offers an industrial application prospect when combined with existing melt blowing devices. However, there are also problems associated with the melt spinning: i) polymer melts have high viscosities, requiring high electric field, and are prone to the risk of electric field breakdown; ii) Most of the melt spun fibers are at the micron level; iii) The device is more complex and requires additional high-temperature heating components, which easily cause electrostatic interferences with high-voltage devices.[25,27] In contrast, solution electrospinning is more suitable for preparing special structures like hollow, porous or core-shell, etc. Therefore, more choices need to involve solution electrospinning. Alternatively, coaxial electrospinning fabrication also frequently applied in the preparation which generated unique core-shell nanostructures with stabilizing effect on interparticle stress and lattice strain caused by particle size growth, enjoying a wide range of popularity.[15,16,28]

The surface of as-prepared electro-spun fibers have many defects, making it necessary to perform post-treatment of the fibers. The commonly used post-treatment is calcination, in which the fiber are treated at high temperatures in inert atmospheres (e.g., N_2, Ar, Ar/H_2) to form carbon coating or in O_2 atmospheres to transform into metal oxides and hybrids. After the calcination, porous structures are usually formed due to the removal of certain components and gas generation.[29] Sui et al. prepared electrospun PAN nanofibers with a homogeneous structure using a multi-step thermal stretching process, and the treated n-CFs were highly aligned and partially graphitized with improved Young's modulus and tensile strength, proving the feasibility of electrospinning.[30] In conclusion, electrospinning is a facile and practical technique for the preparation of nanofibers, which is currently being developed towards multifunctionality and large-scale.

3. Rate Capabilities of SIBs

3.1. Factors affecting the rate capabilities

The rate capability usually refers to the specific capacity, capacity retention, and recovery capability under various charge-discharge current densities, the excellent rate capability represents the better implementation of fast charge/discharge. Basically, the ion diffusion rate of a material is closely related to its rate performance, and the faster the diffusion rate, the better the rate performance follows. Except for the Na^+ diffusion coefficient, the factors that affect the rate capabilities also include the diffusion distance of Na^+ and the electronic conductivity of electrode materials, both of which involve boundary and surface issues of the overall electrode material, as well as macroscopic material morphology design. For the diffusion of Na^+, the characteristic time can be captured by the equation: $\tau = L^2/D$, where L is the characteristic diffusion length of Na^+, which is related to the particle size of the active material, and D is the Na^+ diffusion coefficient in the host material, which depends on the structure of the material.[31] Multidimensional ion channels will facilitate the

Batteries & Supercaps

Review
doi.org/10.1002/batt.202300271

Chemistry
Europe
European Chemical
Societies Publishing

migration of Na^+ in multiple orientations, so that the diffusion of Na^+ in the framework will be facilitated.[32] In terms of the electronic conductivity, it can be divided into "long-range conductivity" and "short-range conductivity". Compared with long-range conductivity, short-range conductivity plays a greater role in improving the rate performance of the battery.[33]

3.2. Advantages of electro-spun materials in improving the rate capabilities of SIBs

Polyanionic cathode materials, especially the NASICON-type materials, have an open 3D framework, which can support large Na^+ insertion/extraction with small deformation, and thus leads to high Na^+ diffusion coefficient.[34] Against the backdrop of high Na^+ diffusion, the low intrinsic conductivity of polyanionic materials becomes particularly prominent, limiting the utilization of their rate performance. Electrospinning represents a facile method to construct 3D conductive networks of interconnected 1D nanofibers and to control the morphology/structure of cathode materials and conductive material decoration such as carbon nanotubes (CNTs), CNFs and graphene (oxide), etc. The electro-spun polyanionic cathode composited with carbon will effectively improve the inherently poor electronic conductivity of polyanionic and thereby enhance their electrochemical performance, especially the rate capability. Besides, electro-spun electrode materials are usually a combination of nano/micron-sized fibrous and similar scale active material particles, and such construction could greatly shorten the Na immigrational distance, accelerating Na^+/e^- transportation, which is also beneficial to the improvement of rate capability. It is worth mentioning that high-rate discharge will cause an increase in the polarization resistance, which will cause excessive heating of the battery or even thermal runaways. Fortunately, the presence of strong X—O covalent bonds improves the stability of O in the lattice and prevents it from being released by oxidation and producing oxygen, which guarantees safer batteries.[12d]

4. Recent Progress of Electro-Spun Polyanionic Cathodes for SIBs

4.1. Mono-polyanion

4.1.1. Vanadium-based polyanion

$Na_3V_2(PO_4)_3$ (NVP) is a representative NASICON-type material with hexagonal crystal system, the $[V_2(PO_4)_3]$ is composed of three PO_4 tetrahedra and two VO_6 octahedra sharing oxygen atoms for linkage, with the Na^+ occupying two unequal Wyckoff sites, one Na^+ in the 6b site (M1) and two are located at the 18e site (M2). For most cases, the reversible sodiation/desodiation only occur at the M2 site while the Na^+ at the M1 site is usually inactive during cycling. Therefore, the reversible capacity is mainly determined by M2 site, corresponding to a theoretical capacity of $117.6\ mAh\,g^{-1}$. Although NVP provides two Na^+ sites, the electron cloud of the

metal is in a discontinuous state limited by the large electronegativity of the polyhedral, which cannot perform direct —M—O—M-electron transfer, resulting in low electronic conductivity.[35] Such low electronic conductivity will result in a decrease in actual specific capacity and poor rate performance, and appropriate modification methods are needed. Liu and coworkers prepared $Na_3V_2(PO_4)_3$ nanoparticles (diameters: 20–30 nm) uniformly embedded in interconnected 1D carbon nanofibers via electrospinning, the NVP-1D CNF cathode shows a discharge capacity of $101\ mAh\,g^{-1}$ at 0.1 C, and exhibiting reversible capacities of $39\ mAh\,g^{-1}$ at 10 C and $20\ mAh\,g^{-1}$ at 20 C, respectively. The efficient conductive network and Na^+ transport channels constructed by 1D nanofibers can sustain high rates of up to 20 C though with low discharge capacity.[36] Li et al. produced 1D $Na_3V_2(PO_4)_3$/C nanorods via electrospinning, when employed as the cathode in SIBs, the 1D $Na_3V_2(PO_4)_3$/C nanorods exhibited a 3.4 V voltage and provided an initial capacity of up to $116.9\ mAh\,g^{-1}$ at 0.05 C. Compared with irregular micron-scale $Na_3V_2(PO_4)_3$/C, the Na^+ diffusion coefficient of $Na_3V_2(PO_4)_3$/C nanorods is calculated to be $5.39\times10^{-13}\ cm^2\,s^{-1}$ that one order of magnitude higher than pristine $Na_3V_2(PO_4)_3$. This work well demonstrates the feasibility of electrospinning and the nanorod morphology prepared from it for enhancing the electrochemical performance of the material.[37] Subsequently, the $Na_3V_2(PO_4)_3$@C nanofibers prepared by Zhou et al. achieved a discharge capacity of $110.6\ mAh\,g^{-1}$ at 0.1 C, and also provided a reversible capacity of $86.5\ mAh\,g^{-1}$ and remained capacity retention of 96% over 100 cycles at 5 C. The excellent electrochemical performances may profit from the constructed 3D carbon network that improve the electronic conductivity of $Na_3V_2(PO_4)_3$ and shorten the length of Na^+ migration.[38] Wu et al. used oxalic acid-assisted electrospinning for pre-reduction, aiming to reduce V^{5+} to V^{3+} and induce the crystallization of $Na_3V_2(PO_4)_3$ with (113) planes by oxalic acid, to further optimize the solution viscosity and electrical conductivity, finally obtaining uniform and smooth $Na_3V_2(PO_4)_3$/C nanofibers. The TEM results clearly illustrated that the single nanofiber composed of $Na_3V_2(PO_4)_3$/C nanoparticles which uniformly embedded in the 1D carbon nanowire, and the $Na_3V_2(PO_4)_3$ nanoparticles were uniformly coated with amorphous carbon layer (~10 nm). The cathode material synthesized with the assistance of oxalic acid is superior, mainly in terms of high rate performance and cycling capability, showing $114\ mAh\,g^{-1}$ at 0.05 C and $78.1\ mAh\,g^{-1}$ at 10 C, and maintaining 97.0% capacity retention after 100 cycles with coulombic efficiency (CE) always close to 100%. In this work, oxalic acid mainly contributes to the following aspects. i) Assisted the synthesis of nanowires with smoother, uniform, and continuous morphology, making $Na_3V_2(PO_4)_3$ uniformly encapsulated in amorphous carbon with a thickness of about 10 nm. ii) Increased the crystal lattice spacing of $Na_3V_2(PO_4)_3$ nanofibers. ii) The R_{ct} of $Na_3V_2(PO_4)_3$/C was greatly reduced, indicating a much faster charge transfer. All the three aspects contribute to favored ion/electron diffusion.[39]

As discussed above, nanocomposites composed of fibrous NVP active material and carbon are favored as cathode materials of SIBs. In addition, the shapes of fibers play a significant role in optimizing their electrochemical performance of the cathodes. On this basis, nanofibers with various structures have been synthe-

Batteries & Supercaps

Review
doi.org/10.1002/batt.202300271

Chemistry Europe
European Chemical
Societies Publishing

sized and studied with the aim of further enhancing the kinetic diffusion of Na$^+$ and achieving better rate performance while maintaining structural stability. Kajiyama et al. calcined the electrospun precursor fibers to prepare a core-sheath structure of Na$_3$V$_2$(PO$_4$)$_3$ nanowire cathode, where Na$_3$V$_2$(PO$_4$)$_3$ crystalline oriented nanoparticles were encapsulated within a carbon sheath. The core-sheath Na$_3$V$_2$(PO$_4$)$_3$ nanowires delivered a discharge capacity of 94 mAh g^{-1} at 1 C and maintained 74% capacity retention over 50 cycles, far better than the bulk one. In addition, the Na$_3$V$_2$(PO$_4$)$_3$ nanowires sustain 86% of the capacity from 0.1 C to 2 C, which is attributed to the mitigating effect of the assembled mesostructured of the oriented Na$_3$V$_2$(PO$_4$)$_3$ nanoparticles on the interparticle stress caused by the particle size growth and the stabilizing effect when the lattice strain was enhanced; Besides, the restriction of the assembly of the nanoparticles within the carbon sheath would facilitate the efficient electron migration pathway during Na$^+$ insertion/extraction.[40] Li et al. synthesized the budded willow-like Na$_3$V$_2$(PO$_4$)$_3$/C fiber, and the rough nanofibers (~250 nm) were intricately interwoven with random orientation, accompanied by many anchored tiny nanoparticles, resembling budding willow branches. (Figure 2a, b). The budded willow-like Na$_3$V$_2$(PO$_4$)$_3$/C compounds delivered a high capacity of 116.2 mAh g^{-1} at 0.05 C, and maintained 107.2 mAh g^{-1} over 125 cycles at 0.2 C, exhibiting excellent cyclability. Besides, the compound delivered 104 mAh g^{-1} at 1 C and 103 mAh g^{-1} at

2 C, respectively (Figure 2c, d). Such close discharge capacities at different rates indicate its exceptional rate capability. Remarkably, unlike the Na$_3$V$_2$(PO$_4$)$_3$/C encapsulated by carbon shell, the strongest relative intensities of the XRD peak of the budded willow-like Na$_3$V$_2$(PO$_4$)$_3$/C material was (113) peak, and the crystal orientation in the (113) plane provides wide and straight channels for Na$^+$ transportation (Figure 2e). Additionally, the thinner bud willow branch carbon layer avoided the hindrance to Na$^+$ transport. Such synergies greatly promote the chemical diffusion of Na$^+$, thus improving the rate capability.[41] Zhu et al. prepared a new structured composite containing Na$_3$V$_2$(PO$_4$)$_3$ nanofibers and Na$_3$V$_2$(PO$_4$)$_3$ nanoparticles (5–10 nm) of carbon nanofibers via coaxial electrospinning, which was denoted as NF-NVP/C. In SIBs, the NF-NVP/C cathode could deliver 108.4, 90.2 and 83.3 mAh g^{-1} at 0.05, 5 and 10 C, respectively. Furthermore, the bipolar NF-NVP/C full batteries shows a high capacity of 106.2 mAh g^{-1} at 0.1 A g^{-1} (voltage window: 0.01–4.00 V), and the corresponding energy density is calculated as 92 Wh kg^{-1}, which considered as competitive in the secondary batteries.[42]

Self-supporting electrodes (also denoted as freestanding electrode) mean that the as-prepared materials can serve as electrodes without adhesives, conductive additives, and current collectors, but also shows great mechanical properties and higher energy density in batteries. The characteristics of electrospinning technology enabled the fabrication of self-supporting electrodes,
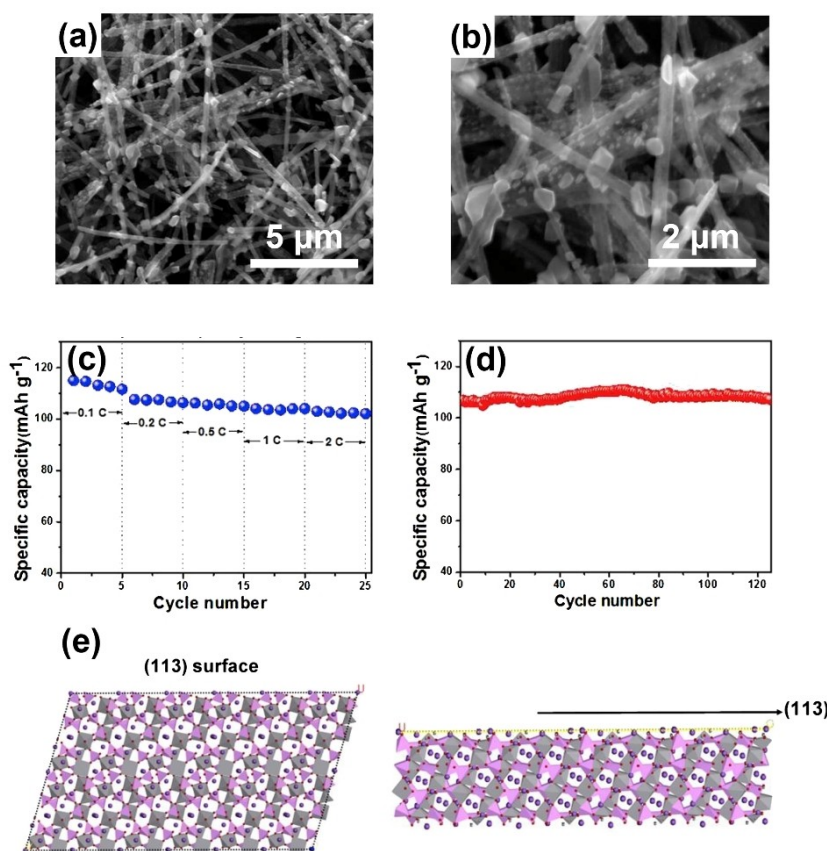
Figure 2. a, b) SEM images of budded willow-like Na$_3$V$_2$(PO$_4$)$_3$/C compounds at different magnifications. c) Rate performance from 0.1 to 2 C and d) cycling performance at 0.2 C of Na$_3$V$_2$(PO$_4$)$_3$/C cathode. e) The atomic arrangements of (113) surface of Na$_3$V$_2$(PO$_4$)$_3$ and the structure viewed perpendicular to (113) surface, respectively. Reproduced with permission from Ref. [41]. Copyright (2015) Elsevier.

thus the pathways of self-supporting vanadium-based phosphate cathode via electrospinning have been explored. For example, Meligrana et al. synthesized the NVP/CNFs composite from electro-spun NVP, and subsequently used dip-coating or Büchner filtration loading methods to obtain the self-supporting NVP-CNFs cathode. Since NVP was directly loaded onto the CNFs support by facile dip coating in the vacuum filtration system without collector and conductive additive, thereby higher energy density was maintained with the advantages of rapid and low cost preparation, worthy of large-scale industrial production. Besides, the self-supporting NVP-CNFs cathode obtained a high initial capacity of

$265\ \mu Ah\,cm^{-2}$, and the battery stabilized at $200\ \mu Ah\,cm^{-2}$ over 70 cycles with high retention of 95% at 1.5 C, exhibiting excellent cycling performance. Superior rate capability of NVP-CNFs cathode can be demonstrated by great specific capacity retention of ~80% at 5 C and ~58% at 10 C.[43] Ni et al. proposed feasible electro-spinning technique to prepare a flexible $Na_3V_2(PO_4)_3/C$ cathodes which possess hierarchical 3D electron channels constructed by thin CNFs (Figure 3a). The as-prepared $Na_3V_2(PO_4)_3/C$ is slender and short with large-sized NVP particle (Figure 3b), and the clear lattice space of 0.65 nm and 0.32 nm detected by HRTEM can be indexed to the (012) and (024) plane, respectively (Figure 3c). In
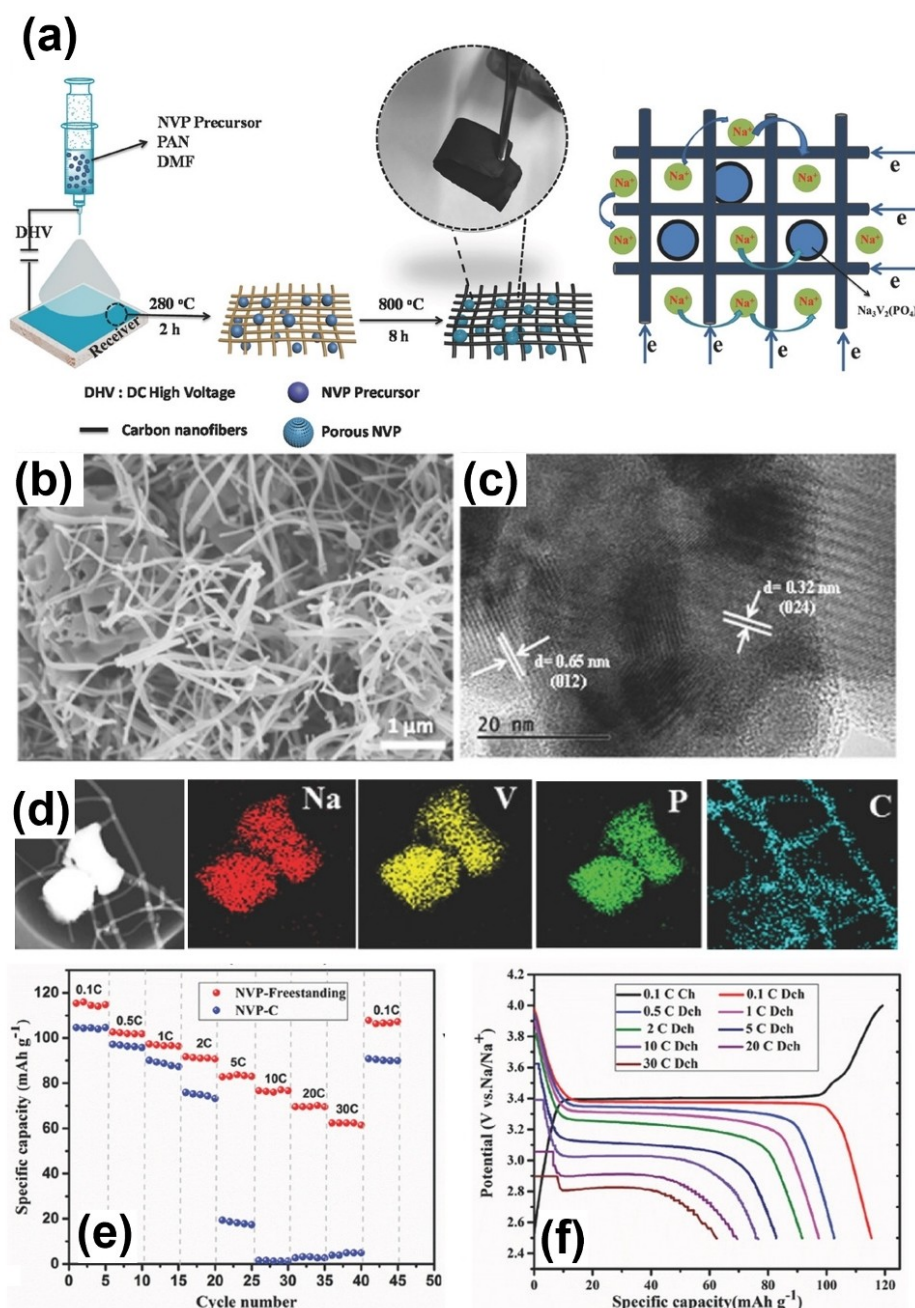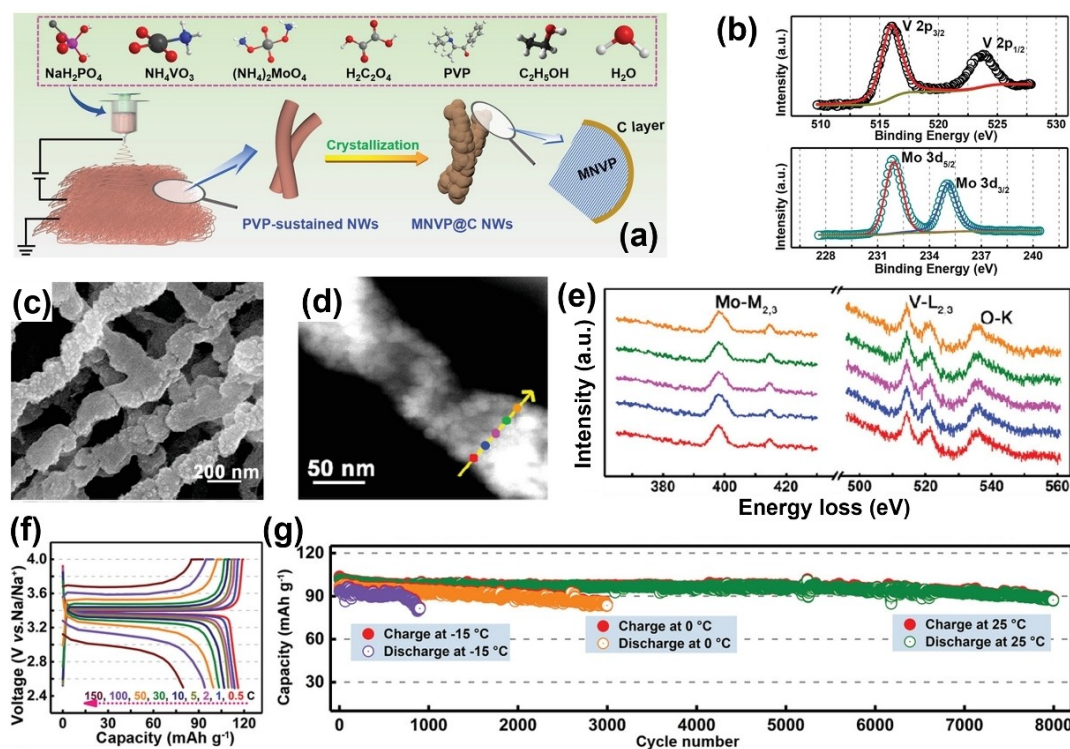

Figure 3. a) Schematic diagram of the fabrication procedure and the transport of Na^+ and e^- in NVP- Freestanding materials, b) SEM and c) HRTEM and d) EDS result of Na, V, P, C element in NVP-Freestanding and e) Rate capacity of NVP-Freestanding and NVP–C. f) Charge-discharge curves of NVP-Freestanding at varying rates. Reproduced with permission from Ref. [44]. Copyright (2018) Wiley-VCH.

addition, the uniform distribution of Na, P, V on NVP particles and the carbon composition of the electro-spun nanofibers were verified through EDS analysis (Figure 3d). The formulated NVP-freestanding electrodes obtained a reversible capacity of 116 mAh g^{-1} at 0.1 C and high rate capacity of 63 mAh g^{-1} at 30 C, which is superior to NVP–C sample (Figure 3e). Besides, Figure 3(f) shows the charge-discharge curves of NVP-Freestanding at different rate, the electrode maintains a low polarization at 0.1–2 C; as the rate increases, the plateau still presents despite the polarization increases. The excellent rate performance of NVP-Freestanding cathode may be profited from its better electrolyte wettability than NVP–C owing to CNFs wrapping as its flexible substrate, accelerating the penetration of electrolyte and the transmission of Na$^+$ between electrodes and within the electrolyte. Additionally, higher electronic conductivity also makes outstanding contributions (8.95 S cm^{-1} of NVPF-Freestanding surpasses 0.252 S cm^{-1} of NVP–C). Furthermore, the packaged NVPF-Freestanding‖Na$_3$Ti$_2$(PO$_4$)$_3$@C sodium full battery obtained an initial discharge capacities of 98 mAh g^{-1} at the 20 mA g^{-1} within the voltage window of 0.4–2.0 V, and the calculated energy density reached 123 Wh kg^{-1} (based on the cathode side).[44] Analogously, Luo et al. synthesized self-standing Na$_3$V$_2$(PO$_4$)$_3$/C fiber membranes by electrospinning, the initial charge/discharge capacities of self-standing Na$_3$V$_2$(PO$_4$)$_3$/C were 117.5 mAh g^{-1} and 107.2 mAh g^{-1}, respectively, corresponding to a high CE of 91.2%. The discharge plateaus were located at 3.37 V. Besides, the self-standing NVP/C retained 100% of the initial capacity over 100 cycles at 0.1 C and maintained an almost constant capacity of 104 mAh g^{-1} in the rate of 0.1 to 5 C, and showed a high rate capacity of 97 mAh g^{-1} at 10 C and 78 mAh g^{-1} at 20 C. The constructed 3D conductive networks possesses a series of merit for enhancing the rate capability of cathodic material: i) Greatly enhances the electronic conductivity of NVP electrode; ii) providing continuous pathway for Na$^+$/e$^-$ transportation and increasing the contact area between electrolyte and electrode; iii) the NVP nanoparticles fixed in the carbon fibers which contribute to shortening the Na$^+$ migration distance and prevent the self-aggregation during cycling.[45]

Heteroatomic doping is a very effective modification method, which often leads to great synergistic effects when combined with electrospinning. Doping effects vary with the doping elements and the doping sites.[46] Yan et al. introduced B dopant and form the configuration of boron groups (BC$_3$, BC$_2$O and BCO$_2$) in the carbon layer of NVP@C composites via electrospinning and carbonization preparation, adjusting the doping amount of B by controlling the amount of boric acid added. In particular, the BC$_2$O helps improves Na$^+$ diffusion while BCO$_2$ aids in enhancing structural stability, so appropriate amounts of BC$_2$O and BCO$_2$ in the composites result in high reversibility and long cyclability of the prepared materials. The optimized electrode material showed a high rate capacity of 103 mAh g^{-1} at 10 C and maintained 91 mAh g^{-1} over 1500 cycles, that is superior to the undoped ones (only 66 mAh g^{-1} at 10 C).[47] Recently, Liang et al. fabricated Mo-doped 1D Na$_3$V$_2$(PO$_4$)$_3$ nanowires (abbreviated as MNVP@C NWs) to be used as multifunctional cathode for Na storage, and fully explored their practicality (Figure 4a). As shown in Figure 4(b), the
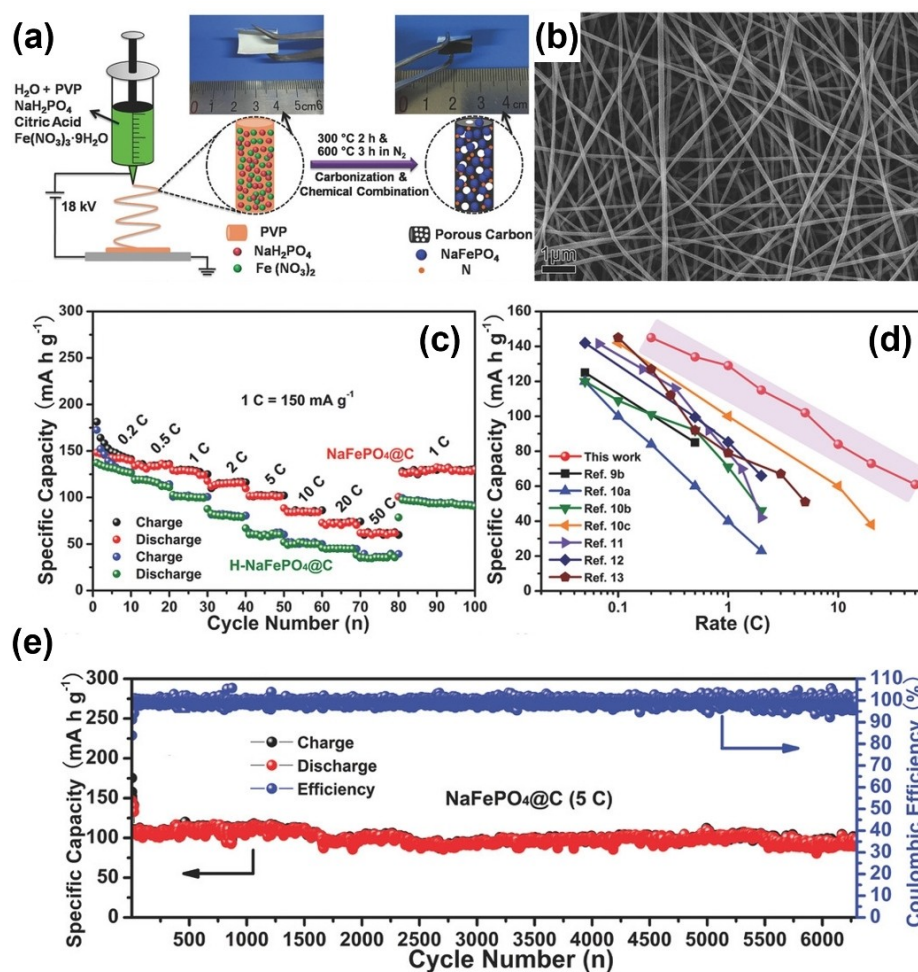

Figure 4. a) Schematic diagram of the preparation process and b) high resolution XPS of V2p and Mo3d and c) SEM and d) HRTEM and e) corresponding EELS spectra of Mo and V of MNVP@C NWs. f) Rate performance of MNVP@C NWs in SIBs. g) Cycling performance of MNVP@C NWs in HLSIBs at different temperatures. Reproduced with permission from Ref. [48]. Copyright (2021) Wiley-VCH.

Batteries & Supercaps

Review
doi.org/10.1002/batt.202300271

Chemistry Europe
European Chemical
Societies Publishing

Mo element can be detected via XPS which indicate the successfully Mo-doped in $Na_3V_2(PO_4)_3$. The SEM image (Figure 4c) clearly reveals that the ultralong nanowires have a rough surface with attached particles (~100 nm). Besides, electron energy loss spectroscopy (EELS) confirmed the uniform distributions of external Mo in nanowires instead of surface doping (Figure 4d, e). For Na storage, the MNVP@C NWs obtained a discharge capacity of 116.8 mAh g^{-1} at 0.1 C. Additionally, the constructed pocket flexible sodium ion batteries (F-SIBs) obtained a large energy density of 262.4 Wh kg^{-1} and an ultra-high rate capability of 77 mAh g^{-1} at 150 C (Figure 4f). And the SIBs exhibit a high capacity of 78.8 mAh g^{-1}, 69.9 mAh g^{-1} and 60.7 mAh g^{-1} at 25 °C, 0 °C and −15 °C, respectively. Besides, the capacity retention of 85.7% after 8000 cycles at 5 C and 25 °C can be achieved (Figure 4g). Functional doping of high-valent Mo^{6+} and conductive carbon layer is considered to be highly necessary to further improve the high rate capability and cycling stability, due to the fact that doped Mo^{6+} can moderately modulate the atomic configuration and lattice structure of $Na_3V_2(PO_4)_3$. In addition, when higher valence doped cations are introduced into the NVP, Na$^+$ vacancies will be generated due to valence equilibrium, and then the electronic conductivity and ion diffusion kinetics of the electrodes are enhanced based on the smaller migration barrier and electrochemical resistance of Na$^+$. Furthermore, for hybrid Li$^+$/Na$^+$ dual-ion storage, the MNVP@C NWs obtained an energy density of 186.1 Wh kg^{-1}, delivering a capacity of 72.1 mAh g^{-1} and 60.5 mAh g^{-1} at the high rate of 30 C and 50 C at 25 °C, respectively. The electrodes also demonstrated excellent cycle stability (e.g., 78.1% over 2600 cycles (55 °C), 84.1% over 3000 cycles (25 °C), and 90.8% after 300 cycles (−25 °C)). The excellent rate capability and long lifespan of electro-spun composites over a wide temperature range, providing new ideas for the rational design of multifunctional cathodes for the new-generation of safe, stable and high-performance rechargeable batteries.[48] Among the groups of vanadium polyanionic materials, $Na_3V(PO_3)_3N$ has the highest voltage plateau of 4.0 V and outstanding rate performance, thus been considered as a charming option for constructing high energy density batteries.[49] Xiao et al. synthesized a novel $Na_3V(PO_3)_3N$ nanofibers via electrospinning, which exhibited superior rate capacity (61.5 mAh g^{-1} at high rate of 50 C) and maintained a satisfactory 86.7% capacity retention over 2000 cycles at 10 C. Based on the electronic energy band structure diagram and density of states (DOS), the conduction band and valence band of $Na_3V(PO_3)_3N$ material exist at the Fermi energy level, which proves that the $Na_3V(PO_3)_3N$ material is a flat band material with s, p, and d orbitals hybridized at the Fermi energy level and has a larger effective mass than other polyanionic materials, leading to the increase of ionic conductivity. Additionally, the DOS is dominated by the d orbitals of V at the Fermi level, which suggests that the involvement of N in this rare cubic structure triggers a larger inductive effect, making the VO$_6$ octahedron more localized.[50]

4.1.2. Iron-based polyanion

The crystal structure of NaFePO$_4$ can be divided into olivine type (o-NaFePO$_4$) and maricite type (m-NaFePO$_4$).[51] In crystal of o-NaFePO$_4$, the FeO$_6$ octahedra and PO$_4$ tetrahedra forms a spatial skeleton with Na$^+$ occupying the co-sided octahedra and a long chain along the b-axis direction.[52] The positions of Na$^+$ and Fe^{2+} in m-NaFePO$_4$ crystals are reversed, but the unchanged position of PO$_4^{3-}$ blocks the Na$^+$ diffusion channel, resulting in poor electrochemical activity.[53] Considering the structural stability of m-NaFePO$_4$, appropriate methods to stimulate its electrochemical activity have been persistently investigated, including the use of electrospinning for synthesis and has made a series of progress. Liu et al. prepared ultra-small NaFePO$_4$ nanodots (~1.6 nm in diameter) uniformly embedded in porous N-doped carbon nanofibers (abbreviated as NaFePO$_4$@C) by electrospinning, and the binder-free NaFePO$_4$@C electrode tightly adhered to Al current collector (Figure 5a, b). The formed porous morphology and nitrogen doping of the carbon nanofibers were introduced due to the released gases and the N-rich feature of polyvinylpyrrolidone (PVP) during the carbonization. In the half-cells, the NaFePO$_4$@C showed high reversible capacity of 145 mAh g^{-1} at 0.2 C and illustrious rate capacity of 61 mAh g^{-1} at 50 C (Figure 5c), which is superior to other reported SIB cathodic materials (Figure 5d). Besides, the NaFePO$_4$@C also exhibited outstanding cyclability with a capacity retention of 89% after 6300 cycles (Figure 5e). The sodium ion full cell composed of NaFePO$_4$@C cathode and CNF anode also displays a remarkable electrochemical performance with the capacity of 124.5 mAh g^{-1} and working voltage of ~2.25 V, corresponds to an energy density of 168.1 Wh kg^{-1} based on the total mass of cathode and anode. The distinctive 3D network effectively increased the utilization of active materials, accelerate the transportation of Na$^+$/e$^-$, and strengthen the overall structural stability during cycling, leading to satisfactory high rate Na-storage capacity.[54] Liu-Théato et al. synthesized a free-standing NaFePO$_4$/CNF (binder-free and current collector-free) via electrospinning the ball-milled NaFePO$_4$ and PAN/DMF solutions. The absence of current collectors and binders facilitated the improvement of the energy density. Furthermore, Mössbauer spectra revealed that the Fe^{3+} content increased from 43.2% at the first charge to 63.0% after 100 cycles, interpreting the nanosizing effect and the fact that the high-potential denaturation process can activate the inactive maricite phase that converts into the active amorphous phase.[55] Chen et al. applied sol-gel pretreatment and electrospinning and roasting to synthesize the homogeneous MFe$_{1-x}$Mn$_x$PO$_4$/NC (M = Li, Na) nanofibers, in which NaFe$_{0.8}$Mn$_{0.2}$PO$_4$/C fibers obtained a high capacity of 134 mAh g^{-1} at 0.1 C and delivered 77 mAh g^{-1} at 5 C, showing high specific capacity and excellent rate capability. In addition, outstanding cycling performance is demonstrated by maintaining a high capacity retention of 88% over 200 cycles at 1 C. The substitution of Fe by Mn and the N-doped amorphous carbon fiber network promotes ion diffusion, surmounting the kinetic limitations and leading to higher redox efficiency of Fe^{2+}/Fe^{3+} during cycling,

Figure 5. a) Schematic diagram of the farbication process and b) SEM image of NaFePO$_4$@C. c) Rate performance of NaFePO$_4$@C and H-NaFePO$_4$@C. d) Comparation of NaFePO$_4$@C and other SIB cathode in rate capacity. e) Cycling performance of NaFePO$_4$@C at 5 C. Reproduced with permission from Ref. [54]. Copyright (2018) Wiley-VCH.

thereby electron conductivity and ion transport efficiency are greatly optimized.[56]

As phosphates readily decompose and dehydrogenate at high temperatures to form high-temperature stable pyrophosphates, such as $Na_{6.24}Fe_{4.88}(P_2O_7)_4$ (denoted as NFPO), a new member of non-toxic and abundant polyanionic compounds with strong P—O bonding possessing electrochemical stability and theoretical capacity of 117.4 mAh g^{-1}, has attracted wide interest. However, the lack of direct metal octahedral interactions leads to its inferior electronical conductivity and higher surface moisture and CO_2 sensitivity predisposes to severe surface oxidation and large initial irreversible capacity.[57] To tackle these challenges, Niu et al. firstly reported a novel graphene-encapsulated $Na_{6.24}Fe_{4.88}(P_2O_7)_4$ composite nanofiber (NFPO@C@rGO). The NFPO covered by a reduced graphene oxide layer exhibited better flexibility which improved Na$^+$/e$^-$ conductivity of the electrode and ensured structural stability during cycling. In addition, further investigation of the pore structure of NFPO@C@rGO revealed the presence of nanofibers with an average pore size of ~2 nm and the largest total pore volume, implying better porosity for electrolyte penetration.

The NFPO@C@rGO delivered 99 mAh g^{-1} over 320 cycles at 40 mA g^{-1} and exhibit capacity of 53.9 mAh g^{-1} at high current (1280 mA g^{-1}), which is 1.6 times higher than the original NFPO@C and the highest reported NFPO in terms of rate performance.[58] The $Na_2Fe(SO_4)_3$ possesses the highest working potential (~3.8 V) among the polyanionic materials with Fe^{3+}/Fe^{2+} redox pairs, but its low electronic conductivity remains to be overcome.[59] Yu et al. first proposed a highly scalable strategy for fabricate the freestanding hybrid membranes $Na_{2+2x}Fe_{2-x}(SO_4)_3$@porous carbon nanofibers (PCNF) with a cycling performance of maintaining >95% of the initial capacity over 500 cycles at the alternating current density of 40 C and 5 C. The porous structure of carbon fibers plays a buffering role and prevents structural deterioration during cycling. Additionally, the balanced layered pores also contribute to the high ion-accessible surface area and low ion transport resistance, which are key to achieving fast electrochemical kinetics and superior high-rate capability in batteries.[60]

Batteries & Supercaps

Review
doi.org/10.1002/batt.202300271

Chemistry Europe
European Chemical
Societies Publishing

4.2. Mixed polyanion

4.2.1. Pyrophosphate-phosphate mixed compounds

The general formula of the pyrophosphate-phosphate hybrid compounds can be expressed as $Na_4M_3(PO_4)_2P_2O_7$ (M=Mn, Fe, Co, Ni), which belong to the orthorhombic crystal structure with the space group of $Pn2_1a$. In $Na_4M_3(PO_4)_2P_2O_7$ framework, the M octahedra are linked to each other in a co-riminal or co-angled manner, the PO_4 tetrahedra are connected to each other by linking these MO_6 octahedra thus forming a lamellar along the direction of the b–c planar units $[M_3P_2O_{13}]_\infty$ and these layered units are linked in the a-axis direction by P_2O_7 groups thereby forming a three-dimensional framework structure. The generated 3D network structure is characterized by the presence of Na^+ diffusion channels along the a, b, c directions. There are four distinct Na sites in this structure, with Na1 and Na4 consisting of NaO_6 octahedra along the b-c plane, whereas the Na2 and Na3 sites are generated by seven-coordinated NaO_7 polyhedra and NaO_6 octahedra along the a-axis.[61]

Practically, the hybrid framework structure of phosphate and pyrophosphate can be stable in sodium ionic compounds, and $Na_4Fe_3(PO_4)_2P_2O_7$ (NFPP) is regarded as a commercially attractive cathodic candidate for SIBs due to the rich resource and low price of raw materials.[62] Zhang et al. prepared a NFPP compounds that $Na_4Fe_3(PO_4)_2P_2O_7$ nanoparticles embedded in carbon nanoribbons (denoted as NFPP–N) via electrospinning and annealing. The NFPP–N cathode shows high rate capacity and long cyclability by delivering 61.2 mAh g^{-1} and maintains capacity retention of 72% over 5000 cycles at 50 C. Distinctively, the NFPP–N cathode also exhibit admirable low temperature adaptability, retains 80.8% of its initial capacity at $-15\,°C$ (75.7 mAh g^{-1}) after 700 cycles at 0.5 C. The unique structure of NFPP–N combines numerous advantages for high rate performance : I) the nanostructure shorten the distance of Na^+ migration, efficiently accelerated electrochemical reaction; II) the carbon nanoribbon improves the inferior electronic conductivity of the NFPP, allowing electron to be transferred in all directions, preventing the self-aggregation and extra side reactions during cycling; III) the 1D nanoribbons interlink into unique 3D networks, which significantly promote the Na^+/e^- transportation.[63] Ren et al. designed a layered carbon decorated $Na_4Fe_3(PO_4)_2P_2O_7$ nanofiber with a hierarchical carbon decoration (denoted as NFPP/C), which provides effective electron and fast ion diffusion pathways (Figure 6a). In Figure 6(b), the carbon nanofibers showed diameters < 200 nm,
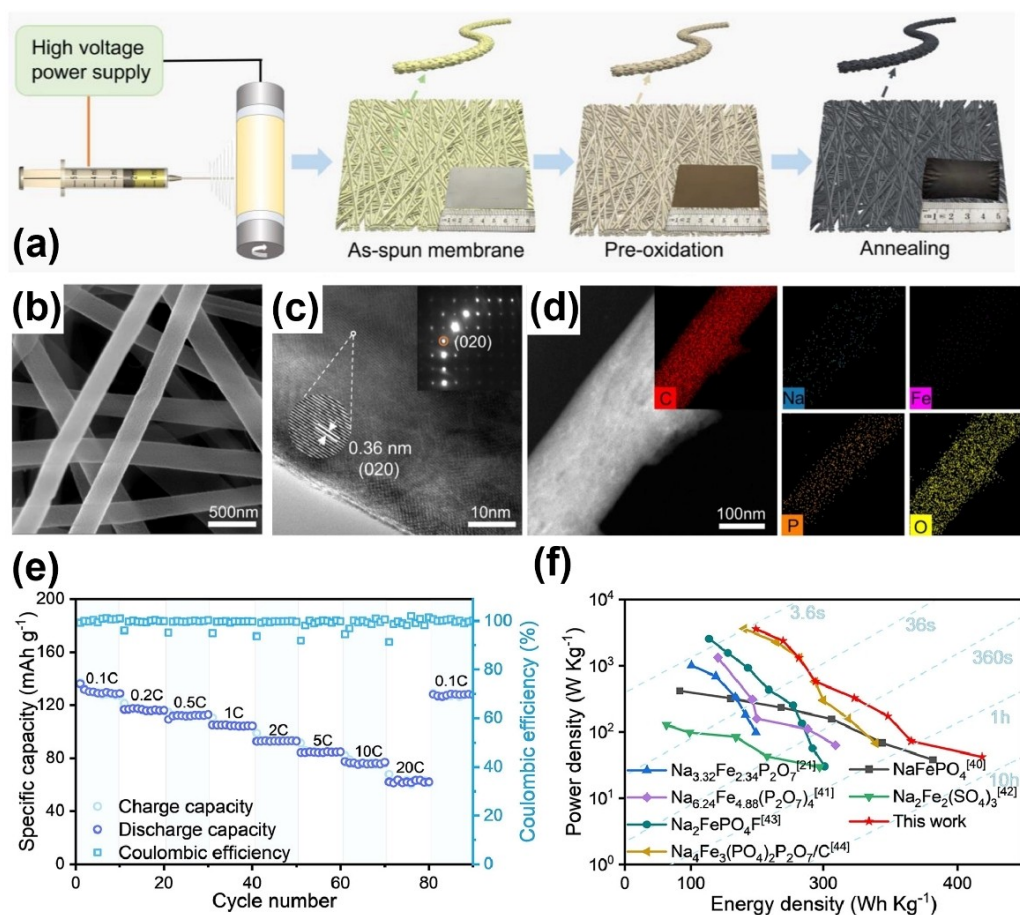
Figure 6. a) Schematic diagram of the preparation process of $Na_4Fe_3(PO_4)_2(P_2O_7)$ nanofiber. b) SEM image, c) HRTEM image, d) EDS, and e) rate performance of $Na_4Fe_3\ (PO_4)_2(P_2O_7)$. f) Comparison of as-prepared $Na_4Fe_3(PO_4)_2(P_2O_7)$ with others reported cathode materials. Reproduced with permission from Ref. [64]. Copyright (2021) Elsevier.

Batteries & Supercaps

Review
doi.org/10.1002/batt.202300271

Chemistry
Europe

European Chemical
Societies Publishing

and the lattice spacing of 0.36 nm corresponds to (020) plane can be observed (Figure 6c). Besides, the elements of Na, Fe, P, O, C are evenly distributed in NFPP/C nanofibers (Figure 6d). In the half cell, the NFPP/C nanofibers exhibit a high reversible capacity of 118 mAhg^{-1} at 0.2 C and high rate capacity of 64 mAhg^{-1} at 20 C (Figure 6e), maintained capacity retention of 79.6% over prolong 10000 cycles at 10 C, and the energy density in different power density are better than other reported iron based polyanionic cathode (Figure 6f). Based on the fitting results of CV and GITT calculations, the Na$^+$ diffusion coefficient of NFPP is as high as 10^{-9} cm^{2}s^{-1}. Besides, through the bond valence sum calculations, the broad distribution and significant overlap of Na$^+$ densities reveal the highly mobile properties of Na$^+$ in the crystalline NFPP, which accelerate the Na$^+$ migration efficiently. Furthermore, the NFPP/C/HC full cell showed a high capacity of 126.4 mAhg^{-1} at 20 mAg^{-1} with a working plateau of 2.9 V. Moreover, it also delivered 95.8 mAhg^{-1} and remained at 70.1 mAhg^{-1} over 180 cycles at 0.1 Ag^{-1}, revealing its commercialization potential in practical applications.[64]

4.2.2. Fluorinated polyanionic compounds

In terms of the redox potential of the polyanionic material explained by molecular orbital theory, where the covalent interaction of M (3d orbital)-O (2sp orbital) splits the molecular orbital into antibonding and bonding orbitals, and when the M—O covalent bond is relatively strong, an enhanced quantum mechanical repulsion arises between the bonding and antibonding orbitals, resulting in the antibonding orbitals being closer to the Na$^+$/Na energy level. The energy difference between these energy levels is decreased, and therefore a lower operating potential is obtained.[12c] If the operating voltage is to be increased, usually an induced effect is used to introduce a more electronegative atom Z (such as O, F, etc.), to form an M—O—Z bond, which biases the electron cloud between the two atoms more toward Z, attaining the weakening of the covalent bonding effect of M—O.[65] Due to the strong inductive effect of PO$_4^{3-}$ and the high electronegativity of F$^-$, the vanadium fluorophosphate (NaVPO$_4$F, Na$_3$V$_2$(PO$_4$)$_2$F$_3$ and Na$_3$V$_2$(PO$_4$)$_2$O$_2$F) have attract great attention with high operating voltage and excellent rate capability.[66] The NaVPO$_4$F presents two different crystal structures: tetragonal structure (space group: *I4/mmm*) and monoclinic structure (space group: *C2/c*). The tetragonal NaVPO$_4$F shows an extended 3D framework consisting of [VO$_4$F$_2$] octahedron and [PO$_4$] tetrahedron for Na$^+$ diffusion, and the monoclinic crystal structure composed of two PO$_4$ tetrahedra sharing two O atoms attached to two different VO$_4$F$_2$ octahedra. As early as 1999, Le Meins and co-worker conducted a systematic study of the structures of the Na$_3$M$_2$(PO$_4$)$_2$F$_3$ family (M=Al^{3+}, V^{3+}, Cr^{3+}, Fe^{3+}, Ga^{3+}), showing that all these compounds emerge the same three-dimensional [M$_3$P$_2$O$_{13}$] network, which consists of a PO$_4$ tetrahedron and a M$_2$O$_8$F$_3$ bio-octahedra formed by the tetragonal corners between the fluorine vertices bridging the two octahedra. Among them, the Na$_3$V$_2$(PO$_4$)$_2$F$_3$ crystallizes in the space group of *P4$_2$/mnm* with

cell parameters of $a=b=9.047(2)$ Å and $c=10.705(2)$ Å. Besides, it can be formed by the substitution of O atoms for partial F atoms in Na$_3$V$_2$(PO$_4$)$_2$F$_3$ ($0 \leq x \leq 1$). For example, the Na$_3$V$_2$(PO$_4$)$_2$O$_2$F has a similar structural framework to Na$_3$(VPO$_4$)$_2$F$_3$ while differs in its cellular parameters of $a=b=6.3811(6)$ Å, $c=10.586(1)$ Å which belongs to the space group of *I4/mmm*.[67] Wherein, the NaVPO$_4$F process the highest theoretical capacity of 143 mAhg^{-1}, moderate voltage plateau of 3.4 V and great structural stability.[68] However, the initial discharge capacity of NaVPO$_4$F early reported by Barker and coworker was only 82 mAhg^{-1} far worse than expectation, and show poor cyclability of remaining capacity retention <50% after only 30 cycles due to the inferior electronic conductivity, which is hard to meet the requirements for practical applications.[69] It is imperative to improve the electrochemical performance of NaVPO$_4$F material. Later on, Jin et al. prepared a self-supporting porous carbon-based NaVPO$_4$F nanofibers via electrospinning (Figure 7a), the diameter of the NaVPO$_4$F nanofibers was measured as 150 nm (Figure 7b) and the uniform and clear lattice fringe of (131) plane can be identified (Figure 7c). The NaVPO$_4$F cathode can deliver a high capacity of 126.3 mAhg^{-1} at 1 C, and shows outstanding rate capability by exhibiting 61.2 mAhg^{-1} at 50 C (Figure 7d). Besides, the long cycling performance of 96.5% capacity retention over 1000 cycles at 2 C can be achieved. The high discharge capacity and long cyclability profited from the nanofibers provided dual continuous electron/ion transport pathways with pores increasing the electrode-electrolyte contact area. Moreover, the 3D conductive network improves the electrical conductivity of NaVPO$_4$F and buffers the self-aggregation of NaVPO$_4$F particles during cycling. Therefore, the optimized NaVPO$_4$F/C exhibits enhanced Na storage capacity.[70] Li et al. prepared a Na$_3$V$_2$(PO$_4$)$_2$F$_3$@N-doped carbon composite nanomaterials (NVPF@C), and the modified NVPF@C material exhibited excellent Na storage performance with a high reversible capacity of 109.5 mAhg^{-1} at 0.1 C, as well as maintained capacity retention of 87.8% and 83.4% after 1000 and 1500 cycles at 20 C and 50 C, respectively. When coupled with hard carbon anode, the NVPF@C||HC full cell can deliver a high energy density of 357.3 Wh kg^{-1} which fully demonstrated its practicality. Besides, the full cell also exhibited 123 Wh kg^{-1} at a high-power density of 15272.7 W kg^{-1}, corresponding to the fast charge/discharge in only 30 s. Such promising electrochemical performance can be contributed to the N doping provides more electrons to the π-conjugated system of carbon, causing an increase in electronic conductivity. At the same time, pyridine N and pyrrole N brings about defects in the carbon nanofibers, effectively expanding the diffusion channels for Na$^+$.[71] Qiu et al. proposed an electrospinning and annealing strategy to encapsulate Na$_3$(VO)$_2$(PO$_4$)$_2$F in carbon nanofibers, enabling it to be able to serve as a flexible electrode. The discharge capacity of CNF@NVPF cathode is 128 mAhg^{-1} at 0.2 C that close to theoretical capacity. Moreover, the CNF@NVPF electrode still maintains 84 mAhg^{-1} at 10 C, surpassing the NVPF electrode (6 mAhg^{-1}). When cycled at 20 C, the CNF@NVPF can still deliver 64.9 mAhg^{-1}, which reflects its superior rate performance. The GITT shows that the
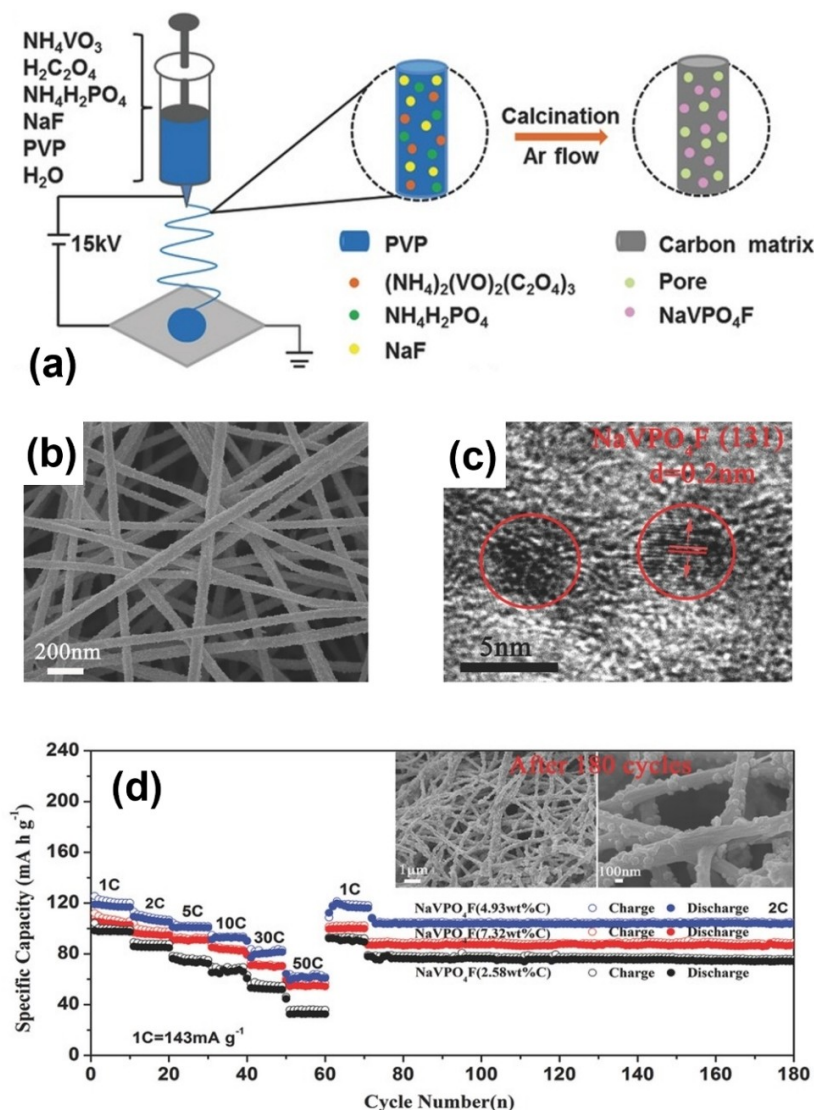
Figure 7. a) Schematic diagram of the fabrication of NaVPO$_4$F nanofiber. b) SEM and c) HRTEM of NaVPO$_4$F and d) rate capability of NaVPO$_4$F-based cathode with different carbon content (inset of SEM about NaVPO$_4$F sample after cycling). Reproduced with permission from Ref. [70]. Copyright (2017) Wiley-VCH.

D_{Na}^+ value of CNF@NVPF electrode is significantly surpass the pure NVPF, enabling the high rate capability. In addition, the CNF@NVPF cathode also demonstrated excellent cyclability with 96% capacity retention over 2000 cycles at 10 C.[72]

In addition to the vanadium based fluorophosphates, other electro-spun transition metal based (Fe, Mn, etc.) fluorophosphates have also been studied. An electro-spun Na$_2$FePO$_4$F nanoparticles (~3.8 nm in diameter) embedded into porous N-doped carbon nanofibers (Na$_2$FePO$_4$F@C) was reported by Wang and coworker (Figure 8a). As shown in Figure 8(b, c), the Na$_2$FePO$_4$F@C nanofibers exhibit diameters of 130 nm and the particle sizes of 3.8 nm. In the half cell, the Na$_2$FePO$_4$F@C cathode obtained a reversible capacity of 117.8 mAh g^{-1} at 1 C with moderate voltage plateau (~3.0 V). In addition, the Na$_2$FePO$_4$F@C maintained 46.4 mAh g^{-1} at high rate of 20 C (Figure 8d) and obtained 85% capacity retention over 2000 cycles (Figure 8e). The large specific area of thin nanofiber and nano Na$_2$FePO$_4$F particles exposes abundant active sites, which

facilitates the easy access of Na$^+$ and the full storage and utilization of Na$^+$. Meanwhile, the nanofibers build a strong 3D network bringing improved electron/ion mobility and structural stability, and the active materials are confined in the porous carbon matrix effectively mitigating the side reactions with the electrolyte. The assembled Na$_2$FePO$_4$F@C||CNF full cells showed a satisfactory energy density of 135.8 Wh kg^{-1} and a reasonable capacity retention of 84.5% after 200 cycles.[73] Despite the help of fluoride, the working platform of Na$_2$FePO$_4$F is not yet ideal because the redox potential is highly correlated with the types of transition metals.[12a] It is noteworthy that the Na$_2$MnPO$_4$F has a high voltage platform of 3.66 V vs. Na/Na$^+$ for the first charge/discharge cycle (4.67 V for the second and so on), which is considered a fascinating cathodic alternative for the construction of high voltage SIBs.[74] For instance, Hu et al. prepared ultra-fine Na$_2$MnPO$_4$F nanoparticles (10–30 nm) confined in 3D carbon nanofibers, which demonstrated a high
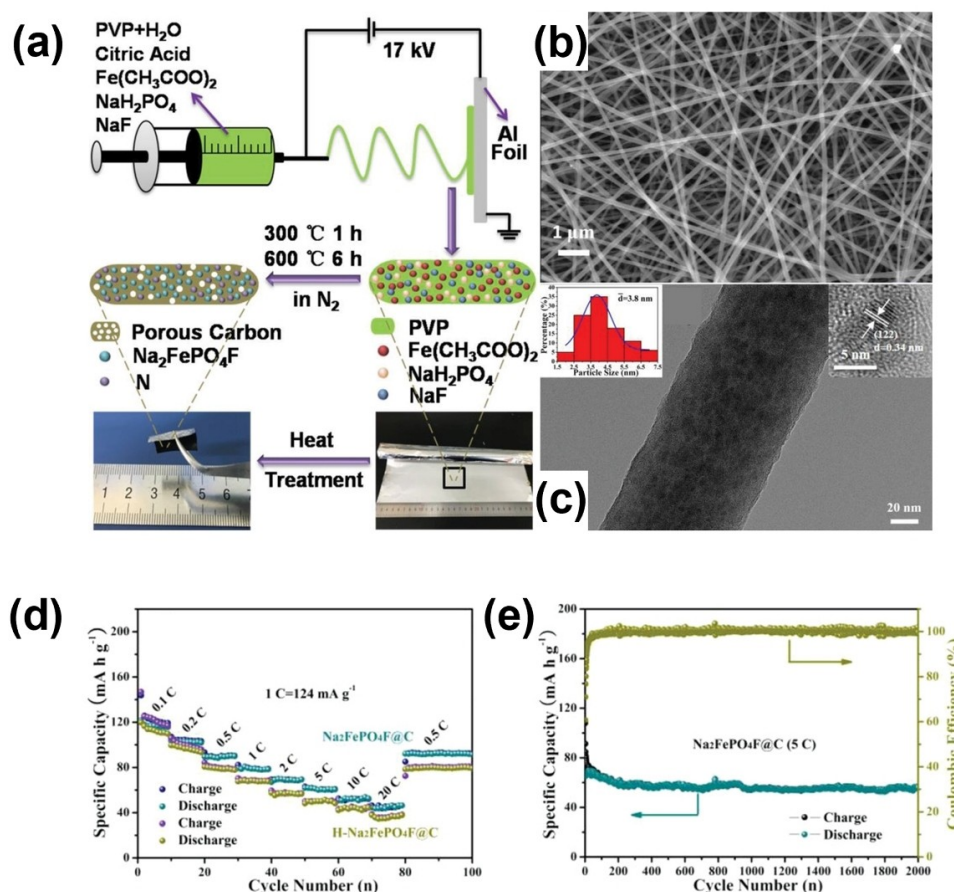
Figure 8. a) Schematic diagram about the preparation of $Na_2FePO_4F@C$ nanofiber. b) SEM and c) HRTEM of $Na_2FePO_4F@C$. d) Rate performance of $Na_2FePO_4F@C$ and $H-Na_2FePO_4F$. e) Cycling performance of $Na_2FePO_4F@C$ at 5 C. Reproduced with permission from Ref. [73]. Copyright (2019) Wiley-VCH.

initial specific capacity of 122.4 mAh g^{-1} at 0.05 C with a working plateau of 3.6 V, approaching the theoretical capacity of Na_2MnPO_4F. Such great electrochemical performance may be attributed to the ultrafine particle size of Na_2MnPO_4F and fast e$^-$/Na$^+$ diffusion in 3D network constructed by compositing with carbon nanofibers.[75] Sui et al. successfully prepared a Na_2MnPO_4F/C nanofibers via pre-oxidation treatment-assisted optimization. Each nanofiber contains Na_2MnPO_4F nanoparticles and a carbon layer/matrix which entangled. The Na_2MnPO_4F/C nanofibers show a high discharge capacity of 122.5 mAh g^{-1} at 0.05 C with the working plateau at 3.5 V which surpasses sample without pre-oxidation by forming a long-chain carbon matrix with a heat-resistant structure. This also reaffirms the positive role of the 3D network structure in favor of promoting electrode reaction kinetics and enhancing reversibility.[76]

5. Conclusions and Perspective

This review summarizes the recent progress of electro-spun polyanionic cathode materials in SIBs, including mono-polyanions (vanadium-based, iron-based) and mixed polyanions (pyrophosphate-phosphate mixed compounds and fluorinated compounds). The use of a facile electrospinning method to

build 3D carbon conductive networks from 1D carbon nanofibers is considered to be an effective method to improve ionic and electronic conductivity of the polyanionic materials, with the following advantages: i) The high specific surface area of nanofibers contributes to larger area of reaction interfaces and more diffusion channels, and the nano- and microsizes of nanofibers provide shorter Na$^+$ diffusion pathways. ii) The gap between aggregated nanoparticles relieves the stress induced during Na$^+$ insertion/desertion. iii) Carbon coating inhibits grain growth and enhances the interparticle and surface electronic conductivity, reducing the polarization of the batteries.

The early studies were mainly devoted to carbon-coated nanofibers prepared by electrospinning, where optimization of the material was limited to carbon coating and nanosizing, demonstrating promising capacity at low rates, but capacity and long cycle life at high rates were less reported. In contrast, recent studies revealed a significant improvement in the rate capability and service life of cathode materials, which was attributed to the combination of multiple modifications, including carbon coating, nanosizing and heteroatomic doping. Although some progress has been made in preparing high-performance polyanionic cathode by electrospinning, there are still issues and challenges remaining to be addressed.

1) The introduction of inactive substances decreases in the specific capacity of the overall electrode, making it difficult to reach the theoretical capacity of active polyanionic materials.

2) The controlling mechanism of nanofibers prepared by electrospinning is ambiguous, whereby the morphology and properties of electro-spun fibers prepared in large scales are far from satisfactory for practical applications.

3) Even though there are diverse polyanionic cathode materials, vanadium-based and iron-based electro-spun fibers are more intensively studied. Other types of polyanionic materials, such as manganese-based, cobalt-based, are less reported, so there is room for further exploration of fabricating high-performance polyanionic cathode materials via electrospinning.

4) Vanadium polyanionic materials, such $Na_3V_2(PO_4)_3$, $NaVPO_4F$, $Na_3V_2(PO_4)_2F_3$ and $Na_3V_2(PO_4)_2O_2F$, etc. contain precious and toxic element "V", partial or complete replacement of V by other environmentally friendly elements, such as Fe and Mn, and ensuring the high-performance of electrode material simultaneously, is highly desired.

With the continuous optimization and modification of materials, it is hoped that the high-performance electro-spun polyanionic cathode can contribute to the development of SIBs, achieving the large-scale energy storage as well as opening a new age of energy reform.

Acknowledgements

Conflict of Interests

The authors declare no conflict of interest.

[1] a) X. B. Cheng, H. Liu, H. Yuan, H. J. Peng, C. Tang, J. Q. Huang, Q. Zhang, *SusMat* **2021**, *1*, 38–50; b) M. Fan, X. Chang, Q. Meng, L. J. Wan, Y. G. Guo, *SusMat* **2021**, *1*, 241–254; c) S. Randau, D. A. Weber, O. Koetz, R. Koerver, P. Braun, A. Weber, E. Ivers-Tiffee, T. Adermann, J. Kulisch, W. G. Zeier, F. H. Richter, J. Janek, *Nat. Energy* **2020**, *5*, 259–270; d) X. Han, Y. Gong, K. Fu, X. He, G. T. Hitz, J. Dai, A. Pearse, B. Liu, H. Wang, G. Rublo, Y. Mo, V. Thangadurai, E. D. Wachsman, L. Hu, *Nat. Mater.* **2017**, *16*, 572–579; e) H. Huang, A. Huang, D. Liu, W. Han, C.-H. Kuo, H.-Y. Chen, L. Li, H. Pan, S. Peng, *Adv. Mater.* **2023**, e2303109; f) L. L. Li, Y. C. Ma, F. Y. Cui, Y. Li, D. S. Yu, X. T. Lian, Y. X. Hu, H. Y. Li, S. J. Peng, *Adv. Mater.* **2023**, *35*, 2209628.

[2] a) M. Fichtner, *Batteries & Supercaps* **2022**, *5*, e202100224; b) Q. Zhao, X. Chen, W. Hou, B. Ye, Y. Zhang, X. Xia, J. Wang, *SusMat* **2022**, *2*, 104–112; c) H. C. Jin, Y. S. Huang, C. N. Wang, H. X. Ji, *Small Sci.* **2022**, *2*, 2200015; d) X. T. Wang, Y. Yang, J. Z. Guo, Z. Y. Gu, E. H. Ang, Z. H. Sun, W. H. Li, H. J. Liang, X. L. Wu, *J. Mater. Sci. Technol.* **2022**, *102*, 72–79.

[3] a) X. M. Xia, K. Z. Chen, S. T. Xu, Y. Yao, L. Liu, C. Xu, X. H. Rui, Y. Yu, *Small Sci.* **2023**, *3*, 2300038; b) R. Usiskin, Y. X. Lu, J. Popovic, M. Law, P. Balaya, Y. S. Hu, J. Maier, *Nat. Rev. Mater.* **2021**, *6*, 1020–1035.

[4] a) D. Gong, C. Wei, Z. Liang, Y. Tang, *Small Sci.* **2021**, *1*, 2100014; b) R. Zhao, N. Sun, B. Xu, *Small Struct.* **2021**, *2*, 2100132; c) J. Zhu, X. Chen, A. Q. Thang, F. L. Li, D. Chen, H. Geng, X. Rui, Q. Yan, *SmartMat* **2022**, *3*, 384–416; d) Y. S. Yu, Y. Yang, F. Tang, S. T. Xu, L. Liu, C. Xu, X. H. Rui, *J. Solid State Electrochem.* **2023**, *27*, 1345–1362; e) S. Ye, L. Wang, F. Liu, P. Shi, Y. Yu, *eScience* **2021**, *1*, 75–82.

[5] C. Vaalma, D. Buchholz, M. Weil, S. Passerini, *Nat. Rev. Mater.* **2018**, *3*, 18013.

[6] K. Chayambuka, G. Mulder, D. L. Danilov, P. H. L. Notten, *Adv. Energy Mater.* **2018**, *8*, 1800079.

[7] a) Z. Hong, H. Maleki, T. Ludwig, Y. Zhen, M. Wilhelm, D. Lee, K.-H. Kim, S. Mathur, *J. Energy Chem.* **2021**, *62*, 660–691; b) Q. Li, D. Yang, H. Chen, X. Lv, Y. Jiang, Y. Feng, X. Rui, Y. Yu, *SusMat* **2021**, *1*, 359–392.

[8] a) T. Y. Wang, D. W. Su, D. Shanmukaraj, T. Rojo, M. Armand, G. X. Wang, *Electrochem. Energy Rev.* **2018**, *1*, 200–237; b) H. Xu, Q. Yan, W. Yao, C.-S. Lee, Y. Tang, *Small Structures* **2022**, *3*, 2100217; c) H. Park, Y. S. Lee, W. Ko, M. Choi, B. Y. Ku, H. Ahn, J. Kim, J. Kang, J. K. Yoo, J. Kim, *Batteries & Supercaps* **2023**, *6*, 2200486; d) Y. J. Fang, L. F. Xiao, Z. X. Chen, X. P. Ai, Y. L. Cao, H. X. Yang, *Electrochem. Energy Rev.* **2018**, *1*, 294–323.

[9] a) Q. Wang, S. Chu, S. Guo, *Chin. Chem. Lett.* **2020**, *31*, 2167–2176; b) Y.-F. Zhu, Y. Xiao, S.-X. Dou, Y.-M. Kang, S.-L. Chou, *eScience* **2021**, *1*, 13–27; c) C. Hakim, N. Sabi, I. Saadoune, *J. Energy Chem.* **2021**, *61*, 47–60; d) J. Feng, S. Luo, K. Cai, S. Yan, Q. Wang, Y. Zhang, X. Liu, *Chin. Chem. Lett.* **2022**, *33*, 2316–2326; e) C. L. Zhao, Q. D. Wang, Z. P. Yao, J. L. Wang, B. Sanchez-Lengeling, F. X. Ding, X. G. Qi, Y. X. Lu, X. D. Bai, B. H. Li, H. Li, A. Aspuru-Guzik, X. J. Huang, C. Delmas, M. Wagemaker, L. Q. Chen, Y. S. Hu, *Science* **2020**, *370*, 708–711.

[10] a) J. F. Qian, C. Wu, Y. L. Cao, Z. F. Ma, Y. H. Huang, X. P. Ai, H. X. Yang, *Adv. Energy Mater.* **2018**, *8*, 1702619; b) S. Zhao, Z. Guo, K. Yan, X. Guo, S. Wan, F. He, B. Sun, G. Wang, *Small Structures* **2020**, *2*, 2000054; c) J. Peng, W. Zhang, Q. Liu, J. Wang, S. Chou, H. Liu, S. Dou, *Adv. Mater.* **2022**, *34*, e2108384.

[11] a) X. P. Yin, S. Sarkar, S. S. Shi, Q. A. Huang, H. B. Zhao, L. M. Yan, Y. F. Zhao, J. J. Zhang, *Adv. Funct. Mater.* **2020**, *30*, 1908445; b) C. Zhang, C. B. Lu, F. Zhang, F. Qiu, X. D. Zhuang, X. L. Feng, *J. Energy Chem.* **2018**, *27*, 86–98.

[12] a) A. Zhao, Y. J. Fang, X. P. Ai, H. X. Yang, Y. L. Cao, *J. Energy Chem.* **2021**, *60*, 635–648; b) P. Barpanda, L. Lander, S.-i. Nishimura, A. Yamada, *Adv. Energy Mater.* **2018**, *8*, 1703055; c) C. Masquelier, L. Croguennec, *Chem. Rev.* **2013**, *113*, 6552–6591; d) T. Jin, H. Li, K. Zhu, P. F. Wang, P. Liu, L. Jiao, *Chem. Soc. Rev.* **2020**, *49*, 2342–2377.

[13] E. Gabriel, C. Ma, K. Graff, A. Conrado, D. Hou, H. Xiong, *eScience* **2023**, 100139.

[14] B. Wang, H. Cai, G. I. N. Waterhouse, X. Qu, B. Yang, S. Lu, *Small Sci.* **2022**, *2*, 2200012.

[15] C. P. Li, M. Qiu, R. L. Li, X. Li, M. X. Wang, J. B. He, G. G. Lin, L. R. Xiao, Q. R. Qian, Q. H. Chen, J. X. Wu, X. Y. Li, Y. W. Mai, Y. M. Chen, *Adv. Fiber Mater.* **2022**, *4*, 43–65.

[16] M. L. Wang, K. Wang, Y. Y. Yang, Y. N. Liu, D. G. Yu, *Polymer* **2020**, *12*, 103.

[17] a) C. L. Zhang, S. H. Yu, *Chem. Soc. Rev.* **2014**, *43*, 4423–4448; b) A. Huang, Y. Ma, J. Peng, L. Li, S.-l. Chou, S. Ramakrishna, S. Peng, *eScience* **2021**, *1*, 141–162.

[18] B. A. Zhang, F. Y. Kang, J. M. Tarascon, J. K. Kim, *Prog. Mater. Sci.* **2016**, *76*, 319–380.

[19] W. H. Li, L. C. Zeng, Y. Wu, Y. Yu, *Sci. China Mater.* **2016**, *59*, 287–321.

[20] L. Wang, G. R. Yang, S. J. Peng, J. N. Wang, W. Yan, S. Ramakrishna, *Energy Storage Mater.* **2020**, *25*, 443–476.

[21] C. F. Armer, J. S. Yeoh, X. Li, A. Lowe, *J. Power Sources* **2018**, *395*, 414–429.

[22] a) Y. Li, J. Zhu, H. Cheng, G. Li, H. Cho, M. Jiang, Q. Gao, X. Zhang, *Adv. Mater. Technol.* **2021**, *6*, 2100410; b) T. J. Sill, H. A. von Recum, *Biomaterials* **2008**, *29*, 1989–2006.

[23] S. J. Peng, G. R. Jin, L. L. Li, K. Li, M. Srinivasan, S. Ramakrishna, J. Chen, *Chem. Soc. Rev.* **2016**, *45*, 1225–1241.

[24] H. G. Wang, S. Yuan, D. L. Ma, X. B. Zhang, J. M. Yan, *Energy Environ. Sci.* **2015**, *8*, 1660–1681.

[25] Y. C. Ding, H. Q. Hou, Y. Zhao, Z. T. Zhu, H. Fong, *Prog. Polym. Sci.* **2016**, *61*, 67–103.

[26] X. X. Wang, G. F. Yu, J. Zhang, M. Yu, S. Ramakrishna, Y. Z. Long, *Prog. Mater. Sci.* **2021**, *115*, 100704.

[27] J. J. Xue, T. Wu, Y. Q. Dai, Y. N. Xia, *Chem. Rev.* **2019**, *119*, 5298–5415.

[28] a) A. M. Al-Dhahebi, J. K. Ling, S. G. Krishnan, M. Yousefzadeh, N. K. Elumalai, M. S. M. Saheed, S. Ramakrishna, R. Jose, *Appl. Phys. Rev.* **2022**, *9*, 011319; b) X. Wen, J. Xiong, S. L. Lei, L. M. Wang, X. H. Qin, *Adv. Fiber Mater.* **2022**, *4*, 145–161.

[29] a) J. Sharma, G. Polizos, C. J. Jafta, D. L. Wood, J. Li, *J. Electrochem. Soc.* **2022**, *169*, 050527; b) T. Blachowicz, A. Ehrmann, *Materials* **2020**, *13*, 152.

[30] G. Sui, F. J. Sun, X. P. Yang, J. Y. Ji, W. H. Zhong, *Compos. Sci. Technol.* **2013**, *87*, 77–85.

[31] N. Balke, S. Jesse, A. N. Morozovska, E. Eliseev, D. W. Chung, Y. Kim, L. Adamczyk, R. E. Garcia, N. Dudney, S. V. Kalinin, *Nat. Nanotechnol.* **2010**, *5*, 749–754.

[32] W. Zong, C. Yang, L. L. Mo, Y. Ouyang, H. L. Guo, L. F. Ge, Y. E. Miao, D. W. Rao, J. W. Zhang, F. L. Lai, T. X. Liu, *Nano Energy* **2020**, *77*, 105189.

[33] S. L. Morelly, N. J. Alvarez, M. H. Tang, *J. Power Sources* **2018**, *387*, 49–56.

[34] a) Z. Jian, Y. S. Hu, X. Ji, W. Chen, *Adv. Mater.* **2017**, *29*, 1601925; b) Y. Liu, J. Li, Q. Shen, J. Zhang, P. He, X. Qu, Y. Liu, *eScience* **2022**, *2*, 10–31; c) S. Q. Chen, C. Wu, L. F. Shen, C. B. Zhu, Y. Y. Huang, K. Xi, J. Maier, Y. Yu, *Adv. Mater.* **2017**, *29*, 1700431.

[35] a) X. Rui, W. Sun, C. Wu, Y. Yu, Q. Yan, *Adv. Mater.* **2015**, *27*, 6670–6676; b) L. Y. Shen, Y. Li, S. Roy, X. P. Yin, W. B. Liu, S. S. Shi, X. Wang, X. M. Yin, J. J. Zhang, Y. F. Zhao, *Chin. Chem. Lett.* **2021**, *32*, 3570–3574; c) Q. Zheng, H. M. Yi, X. F. Li, H. M. Zhang, *J. Energy Chem.* **2018**, *27*, 1597–1617; d) R. Sun, X. C. Guo, S. Y. Dong, C. H. Wang, L. X. Zeng, S. J. Lu, Y. F. Zhang, H. S. Fan, *J. Power Sources* **2023**, *567*, 232946; e) X. T. Li, H. J. Liang, B. Y. Qin, M. Q. Wang, Y. F. Zhang, H. S. Fan, *J. Colloid Interface Sci.* **2022**, *625*, 41–49.

[36] J. Liu, K. Tang, K. P. Song, P. A. van Aken, Y. Yu, J. Maier, *Nanoscale* **2014**, *6*, 5081–5086.

[37] H. Li, Y. Bai, F. Wu, Q. Ni, C. Wu, *Solid State Ionics* **2015**, *278*, 281–286.

[38] Z. F. Zhou, N. Li, C. Zhang, X. Chen, F. Xu, C. Peng, *Solid State Ionics* **2018**, *326*, 77–81.

[39] L. Wu, S. N. Shi, X. P. Zhang, Y. Yang, J. Q. Liu, S. B. Tang, S. K. Zhong, *Electrochim. Acta* **2018**, *274*, 233–241.

[40] S. Kajiyama, J. Kikkawa, J. Hoshino, M. Okubo, E. Hosono, *Chem. Eur. J.* **2014**, *20*, 12636–12640.

[41] H. Li, Y. Bai, F. Wu, Y. Li, C. Wu, *J. Power Sources* **2015**, *273*, 784–792.

[42] Q. Zhu, B. Nan, Y. Shi, Y. G. Zhu, S. S. Wu, L. Q. He, Y. H. Deng, L. P. Wang, Q. Q. Chen, Z. G. Lu, *J. Solid State Electrochem.* **2017**, *21*, 2985–2995.

[43] G. Meligrana, S. Ferrari, L. Lucherini, J. Cele, F. Colo, J. Brugger, C. Ricciardi, R. Ruffo, C. Gerbaldi, *ChemElectroChem* **2020**, *7*, 1652–1659.

[44] Q. Ni, Y. Bai, Y. Li, L. M. Ling, L. M. Li, G. H. Chen, Z. H. Wang, H. X. Ren, F. Wu, C. Wu, *Small* **2018**, *14*, 1702864.

[45] L. L. Luo, B. Cheng, S. J. Chen, Z. C. Ge, H. T. Zhuo, *Mater. Lett.* **2018**, *232*, 153–156.

[46] Y. Li, M. Chen, B. Liu, Y. Zhang, X. Liang, X. Xia, *Adv. Energy Mater.* **2020**, *10*, 2000927.

[47] D. Yan, S. H. Xiao, X. Y. Li, R. Wu, J. X. Jiang, X. B. Niu, J. S. Chen, *ChemSusChem* **2022**, *15*, e202201121.

[48] L. W. Liang, X. Y. Li, F. Zhao, J. Y. Zhang, Y. Liu, L. R. Hou, C. Z. Yuan, *Adv. Energy Mater.* **2021**, *11*, 2100287.

[49] J. Kim, G. Yoon, M. H. Lee, H. Kim, S. Lee, K. Kang, *Chem. Mater.* **2017**, *29*, 7826–7832.

[50] J. Xiao, W. B. Hua, M. Z. Chen, *Nanotechnology* **2021**, *32*, 435404.

[51] K. Zaghib, J. Trottier, P. Hovington, F. Brochu, A. Guerfi, A. Mauger, C. M. Julien, *J. Power Sources* **2011**, *196*, 9612–9617.

[52] W. Tang, X. H. Song, Y. H. Du, C. X. Peng, M. Lin, S. B. Xi, B. B. Tian, J. X. Zheng, Y. P. Wu, F. Pan, K. P. Loh, *J. Mater. Chem. A* **2016**, *4*, 4882–4892.

[53] G. Ali, J. H. Lee, D. Susanto, S. W. Choi, B. W. Cho, K. W. Nam, K. Y. Chung, *ACS Appl. Mater. Interfaces* **2016**, *8*, 15422–15429.

[54] Y. C. Liu, N. Zhang, F. F. Wang, X. B. Liu, L. F. Jiao, L. Z. Fan, *Adv. Funct. Mater.* **2018**, *28*, 1801917.

[55] X. Liu-Theato, S. Indris, W. B. Hua, H. Li, M. Knapp, G. Melinte, H. Ehrenberg, *Energy Fuels* **2021**, *35*, 18768–18777.

[56] W. Y. Chen, D. H. Xu, Y. C. Chen, T. Tang, S. J. Kuang, H. K. Fu, W. Y. Zhou, X. Y. Yu, *Adv. Mater. Interfaces* **2020**, *7*, 2000684.

[57] Y. B. Niu, M. W. Xu, S. J. Bao, C. M. Li, *Chem. Commun.* **2015**, *51*, 13120–13122.

[58] Y. B. Niu, M. W. Xu, C. L. Dai, B. L. Shen, C. M. Li, *Phys. Chem. Chem. Phys.* **2017**, *19*, 17270–17277.

[59] P. Barpanda, G. Oyama, S. Nishimura, S. C. Chung, A. Yamada, *Nat. Commun.* **2014**, *5*, 4358.

[60] T. T. Yu, B. Lin, Q. F. Li, X. H. Wang, W. L. Qu, S. Zhang, C. Deng, *Phys. Chem. Chem. Phys.* **2016**, *18*, 26933–26941.

[61] a) S. Ryu, J. E. Wang, J. H. Kim, R. Ruffo, Y. H. Jung, D. K. Kim, *J. Power Sources* **2019**, *444*, 227274; b) B. Senthilkumar, C. Murugesan, L. Sharma, S. Lochab, P. Barpanda, *Small Methods* **2018**, *3*, 1800253.

[62] a) X. J. Pu, H. M. Wang, T. C. Yuan, S. N. Cao, S. Y. Liu, L. Xuc, H. X. Yang, X. P. Ai, Z. X. Chen, Y. L. Cao, *Energy Storage Mater.* **2019**, *22*, 330–336; b) A. L. Zhao, C. Y. Liu, F. J. Ji, S. H. Zhang, H. M. Fan, W. H. Ni, Y. J. Fang, X. P. Ai, H. X. Yang, Y. L. Cao, *ACS Energy Lett.* **2023**, *8*, 753–761.

[63] J. H. Zhang, L. B. Tang, Y. Zhang, X. Q. Li, Q. J. Xu, H. M. Liu, Z. F. Ma, *J. Power Sources* **2021**, *498*, 229907.

[64] W. Ren, M. Qin, Y. Zhou, H. Zhou, J. Zhu, J. Pan, J. Zhou, X. Cao, S. Liang, *Energy Storage Mater.* **2023**, *54*, 776–783.

[65] L. Zhu, H. Wang, D. Sun, Y. Tang, H. Wang, *J. Mater. Chem. A* **2020**, *8*, 21387–21407.

[66] a) S. T. Xu, Y. Yang, F. Tang, Y. Yao, X. Lv, L. Liu, C. Xu, Y. Z. Feng, X. H. Rui, Y. Yu, *Mater. Horiz.* **2023**, *10*, 1901–1923; b) K. Liang, D. Wu, Y. Ren, X. Huang, J. Ma, *Chin. Chem. Lett.* **2022**, *34*, 107978; c) Z.-Y. Gu, J.-Z. Guo, Z.-H. Sun, X.-X. Zhao, X.-T. Wang, H.-J. Liang, X.-L. Wu, Y. Liu, *Cell Rep. Phys. Sci.* **2021**, *2*, 100665.

[67] J. M. Le Meins, M. P. Crosnier-Lopez, A. Hemon-Ribaud, G. Courbion, *J. Solid State Chem.* **1999**, *148*, 260–277.

[68] M. Law, P. Balaya, *Energy Storage Mater.* **2018**, *10*, 102–113.

[69] M. Ling, F. Li, H. Yi, X. Li, G. Hou, Q. Zheng, H. Zhang, *J. Mater. Chem. A* **2018**, *6*, 24201–24209.

[70] T. Jin, Y. C. Liu, Y. Li, K. Z. Cao, X. J. Wang, L. F. Jiao, *Adv. Energy Mater.* **2017**, *7*, 1700087.

[71] Y. Li, X. Liang, G. Zhong, C. Wang, S. Wu, K. Xu, C. Yang, *ACS Appl. Mater. Interfaces* **2020**, *12*, 25920–25929.

[72] R. Y. Qiu, R. X. Fei, J. Z. Guo, R. Wang, B. B. He, Y. S. Gong, X. L. Wu, H. W. Wang, *J. Power Sources* **2020**, *466*, 228249.

[73] F. F. Wang, N. Zhang, X. D. Zhao, L. X. Wang, J. Zhang, T. S. Wang, F. F. Liu, Y. C. Liu, L. Z. Fan, *Adv. Sci.* **2019**, *6*, 1900649.

[74] L. Wu, Y. Hu, X. P. Zhang, J. Q. Liu, X. Zhu, S. K. Zhong, *J. Power Sources* **2018**, *374*, 40–47.

[75] Y. Hu, L. Wu, G. X. Liao, Y. Yang, F. Ye, J. B. Chen, X. Zhu, S. K. Zhong, *Ceram. Int.* **2018**, *44*, 17577–17584.

[76] Y. L. Sui, Z. H. Shi, Y. Hu, X. P. Zhang, X. W. Wu, L. Wu, *J. Colloid Interface Sci.* **2021**, *603*, 430–439.